Thesis for the degree of Doctor of Philosophy

Millimetre wave waveguide enclosed grid frequency multipliers and imaging

Robin Dahlbäck

Terahertz and Millimetre Wave Laboratory
Department of Microtechnology and Nanoscience (MC2)
Chalmers University of Technology
Göteborg, Sweden, 2016

Millimetre wave waveguide enclosed grid frequency multipliers and imaging

Robin Dahlbäck

ISBN 978-91-7597-407-1

Doktorsavhandlingar vid Chalmers tekniska högskola
Ny serie nr 4088
ISSN 0346-718X

Technical Report MC2-339
ISSN 1652-0769

Department of Microtechnology and Nanoscience - MC2
Terahertz and Millimetre Wave Laboratory
Chalmers University of Technology
SE-412 96 Göteborg
Sweden
Phone: +46 (0) 31 772 1000

Front cover illustration: A photograph of two grid frequency multiplier modules.

Printed by Chalmers Reproservice, Göteborg
Göteborg, Sweden, May, 2016

Millimetre wave waveguide enclosed grid frequency multipliers and imaging

Robin Dahlbäck
Chalmers University of Technology
Department of Microtechnology and Nanoscience - MC2
Terahertz and Millimetre Wave Laboratory
SE-412 96 Göteborg
Sweden

Abstract

The utilisation of the THz spectrum (0.3-10 THz) is hampered by fundamental difficulties in generating power at these frequencies. Applications within such diverse fields as radio astronomy, security imaging, life sciences, high data rate communications and production monitoring could benefit significantly from compact, high power THz signal sources operating at room temperature. This thesis reports on the design and fabrication aspects of varactor diode based waveguide enclosed grid frequency multipliers. The goal of this work has been to design, fabricate and characterise high power varactor grid frequency multipliers, enabling increased power handling capabilities and output power of future THz frequency multipliers. This approach is expected to offer excellent frequency and power scalability for THz signal sources.

A tunable 240 - 290 GHz 72 element grid HBV frequency tripler is presented together with measurement data. With an output power of 35 mW at 247 GHz this is the highest frequency of operation reported to date for waveguide enclosed grid frequency multipliers. Furthermore, a 128 Schottky diode frequency doubler grid is presented, with a measured peak output power of 0.25 W at 183 GHz. With a peak conversion efficiency of 23 % it is the most efficient waveguide enclosed grid multiplier reported to date. A modelling approach using parallel sets of cascaded unit cells has been successfully developed as well as a full 3D simulation for grid frequency multipliers.

Two application examples that could benefit from future high power THz sources are also presented. The first one is a 346 GHz imaging system using an imaging algorithm based on the Born approximation to produce images with a sub wavelength pixel size of $0.1 \times 0.1\ mm^2$. The second application example is a FMCW radar transceiver operating at 340 GHz, packaged into a compact modular system designed for array integration.

Keywords: 2D-grid, Array, FMCW, Frequency multipliers, Grid, Heterostructure Barrier Varactors (HBVs), Millimeter wave, Varactors, Radars, Schottky diodes, sub-millimetre waves, THz imaging, THz sources, Quasi-optical.

List of appended papers

This thesis is based on the following appended papers:

[A] **R. Dahlbäck**, J. Vukusic, R.M. Weikle II, and J. Stake, "A tunable 240 — 290 GHz waveguide enclosed 2D-grid HBV frequency tripler," *IEEE Transactions on Terahertz Science and Technology*, vol. 6, no. 3, May 2016.

[B] **R. Dahlbäck**, V. Drakinskiy, J. Vukusic and J. Stake, "A compact 128 Schottky diode grid frequency doubler generating 0.25 W of output power at 183 GHz.," submitted to *IEEE Microwave and Wireless Components Letters*, April 2016.

[C] G. Hrubó, **R. Dahlbäck**, and J. Stake, "Full 3D Modeling of Waveguide Embedded Frequency Multiplier Arrays.," submitted to *IEEE Microwave and Wireless Components Letters*, March 2016.

[D] **R. Dahlbäck**, T. Rubaek, M. Persson, and J. Stake, "A System for THz Imaging of Low-Contrast Targets Using the Born Approximation," *IEEE Transactions on Terahertz Science and Technology*, vol. 2, no. 3, pp. 361-370, April 2012.

[E] **R. Dahlbäck**, G. Granström, M. Ferndahl, V. Drakinskiy, T. Bryllert, and J. Stake, "Compact 340 GHz homodyne transceiver modules for FMWC imaging radar arrays," *International Microwave Symposium*, May 2016, San Francisco, CA, USA.

The following publications are not included due to an overlap in contents or the fact that the contents are beyond the scope of this thesis:

[F] J. Garcia-Wernersson, H. Rodilla, A. Diaz-Bolado, **R. Dahlbäck**, L. Gradinarsky, M. Josefson and J. Stake, "Non-destructive density control of pharmaceutical compounds by THz imaging," Submitted to *Infrared Millimeter and Terahertz Waves (IRMMW-THz), 35th International Conference on*, Sep. 2016.

[G] **R. Dahlbäck**, J. Vukusic, R.M. Weikle II, and J. Stake, "A Waveguide Embedded 250 GHz Frequency-Tripler 2D Array," Micro- and Millimetre Wave Technology and Techniques Workshop, Nov. 2014.

[H] **R. Dahlbäck**, J. Vukusic, R.M. Weikle II, and J. Stake, "A waveguide embedded 250 GHz quasi-optical frequency-tripler array," EuMC, Oct. 2014.

[I] J. Stake, H. Zhao, V. Drakinskiy, T. Bryllert, A Malko, J. Hanning, A.Y. Tang, P. Sobis, **R. Dahlbäck**, and J. Vukusic, "Integrated diode technology for THz applications," Presented at the *SPIE Optics+ Photonics, Terahertz Emitters, Receivers, and Applications IV*, Aug. 2013.

[J] J. Stake, T. Bryllert, **R. Dahlbäck**, V. Drakinskiy, J. Hanning, A Malko, A.Y. Tang, J. Vukusic, H. Zhao and P. Sobis, "Integrated terahertz electronics for imaging and sensing," Presented at the *Microwave Radar and Wireless Communications (MIKON), 19th International Conference on*, May. 2012.

[K] T. Rubæk, **R. Dahlbäck**, A. Fhager, M. Persson and J. Stake, "A single-channel THz imaging system for biomedical applications," Presented at the *General Assembly and Scientific Symposium, URSI* , Aug. 2011.

[L] **R. Dahlbäck**, J. Vukusic and J. Stake, "Development of a waveguide integrated sub-millimetre wave spatially power combined HBV multiplier," Poster presented at the *6th ESA Workshop on Millimetre-Wave Technology and Applications and 4th Global Symposium on Millimeter Waves*, May. 2011.

[M] T. Rubæk, **R. Dahlbäck**, A. Fhager, J. Stake and M. Persson, "A THz imaging system for biomedical applications," Presented at the *5th European Conference on Antennas and Propagation, EUCAP*, Apr. 2011.

[N] **R. Dahlbäck**, T. Rubæk, T. Bryllert, M. Persson, and J. Stake, "A 340 GHz CW non-linear imaging system," Poster presented at the *Infrared Millimeter and Terahertz Waves (IRMMW-THz), 35th International Conference on*, Sep. 2010.

[O] **R. Dahlbäck**, B. Banik, P. Sobis, A. Fhager, M. Persson, and J. Stake, "A Compact 340 GHz Heterodyne Imaging System," Presented at the *GigaHertz Symposium*, Mar. 2010.

Thesis

As a part of the author's doctoral studies, some work presented in this thesis has previously been published in [P]. Material from [P] may therefore be fully or partly reproduced in this thesis.

[P] **R. Dahlbäck** "HBV frequency multiplier 2D arrays and application," Tekn. Lic. Thesis, Departement of Microtechnology and Nanoscience, Chalmers University of Technology, Göteborg, 2014

Table of Contents

Acronyms

2D two dimensional. 5, 6
3D three dimensional. 5

AlAs Aluminum Arsenide. 9

DC direct current. 8

EM electro magnetical. 20
EMF induced electromagnetic force. 20

FMCW Frequency Modulated Continuous Wave. 17

GaAs Gallium Arsenide. 6
GaN Gallium Nitride. 5, 6
GHz Gigahertz. 3, 5, 6

H10 H10 waveguide mode, also known as TE10. 16, 22, 23, 52
HBV Heterostructure Barrier Varactor. 3, 4, 6–8, 10, 12, 13

InAlAs Indium Aluminum Arsenide. 6
InGaAs Indium Gallium Arsenide. 6

MMIC Monolithic Microwave Integrated Circuit. 6

NMR Nuclear Magnetic Resonance spectroscopy. 5

OMT orthomode transducer. 18

QCL quantum cascade laser. 4

RADAR Radio Detection and Ranging. 5
RF radio frequency. 18

Rx received signal. 18

THz Terahertz. 3–7, 11
Tx transmitted signal. 18

List of notations

A Device area. 10
a Fitting parameter. 12

b Barrier thickness. 10
β Fitting parameter. 12

C Capacitance. 8
C_{j0} Zero bias junction capacitance. 12
C_{max} Maximum capacitance. 10

E_0 Fitting parameter. 12
E_b Electric field strength in the barrier. 12
ε_b Relative permittivity of the barrier region. 10
ε_d Relative permittivity of the modulation region. 10
η Ideality factor. 12

$f_{n\times p}$ n:th harmonic of the pump frequency. 8
f_p Pump frequency. 8

I Current. 12
I_0 Saturation current. 12

k Boltzmann constant. 10

L_d Debye length. 10, 12

N Number of barriers. 10
C_{max} Maximum capacitance. 10
n_{mult} Multiplication factor. 7

ϕ_b Fitting parameter. 12

$P_{out,unit\ \ cell\ col\ n}$ Output power from a unit cell in column n. 23
ψ_{bi} Built in potential. 11

Q Stored charge. 11
q Elementary charge. 10
q_{max} Maximum charge. 11

R_s Series resistance. 8, 12

S Elastance. 8
s Spacer thickness. 10
S_{max} Maximum elastance. 11
S_{min} Minimum elastance. 11

T Physical temperature of the device. 10

V_d Voltage across the diode. 10
V_{HBV} Voltage across the HBV varactor. 11

w Depletion layer width. 10

Chapter 1

Introduction

The Terahertz (THz) region is one of the last unconquered parts of the electromagnetic spectrum. The difficulty of using this part of the spectrum comes from the fact that the frequency is very high in electronic terms but at the same time very low in the optical perspective; the terahertz gap is squeezed in between microwaves and visible light. The Terahertz region of the electromagnetic spectrum is generally defined as 300 Gigahertz (GHz) ($\lambda = 1\ mm$; photon energy = $1.2\ meV$) to 10 THz ($\lambda = 0.03\ mm$; photon energy = $41\ meV$). When approaching the Terahertz region from the electronics side devices are hampered by the transit times of electrons in the materials. Similarly challenging is to lower the frequency of optical devices, a THz laser based on an energy transition would require a transition energy of the same order as the room temperature lattice vibrations in the material. Significant research effort is put into overcoming these limitations and ultimately bridging the terahertz gap.

Research on THz technology, was initiated by J. C. Bose who during the 1890's created the forerunner to modern diode detectors with his 60 GHz galena receiver [1]. The development of THz electronics has long been led by the radioastronomy community, but is nowadays finding its way into a broader range of applications, e.g., medical research [2], production monitoring [3], spectroscopy [4–11], non-invasive inspection [12, 13] and security applications [14–17]. Common for all those fields is the lack of compact, efficient and affordable signal sources and detectors.

In this work two semiconductor devices are used to construct signal sources in the form of frequency multipliers, the Schottky diode and the Heterostructure Barrier Varactor (HBV) diode. A Schottky diode is formed at the interface of a metal-semiconductor contact. The Schottky diode has a long heritage within the electronics community, the first experimental results were presented 1874 by Braun [20]. Applications of the metal-semiconductor rectifier followed during the coming years but it was

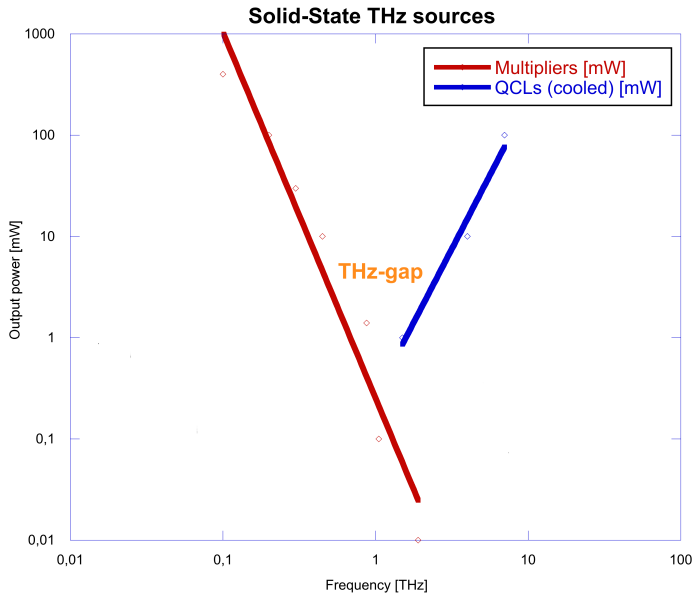

Figure 1.1: Output power levels for state-of-the-art sources, solid-state devices, in the THz frequency range [18, 19]. The term THz-gap is often used to describe the lack of powerful sources at THz frequencies.

not until 1931 when Willson [21] formulated the transport theory of semiconductors based on the band theory of solids that a theoretical foundation started to form. In 1938 Schottky [22] proposed that the potential barrier could arise form space charges in the semiconductor and in 1942 Bethe [23] presented what was to become the thermionic emission model describing the dominant carrier transport mechanism in the Schottky diode. Semiconductor heterojunctions, the fundamental building block of HBV varactors were proposed in 1951 by Shockley and Gubanov [24, 25]. In 1989 Kollberg and Rydberg [26] proposed the Quantum-barrier-varactor diode that later became known as the HBV diode.

Todays power generation devices operating in the THz spectrum can be categorised into two main groups, electronics based devices and photonics based devices. The electronics based devices can further be subdivided into semiconductor devices and vacuum devices. The work presented here falls into the first category, in which its distinctive characteristics are that power is generated in a semiconductor, typically a diode or a transistor, and the circuit is designed using methods common for the microwave electronics community. Vacuum devices utilise the interaction of a relativistic electron beam with a slow wave structure to generate or amplify THz radiation [27]. A photonics based device could be a semiconductor crystal where the THz generation comes

from photo mixing, or a quantum cascade laser (QCL) [18, 19] One of the main advantages of electronics based sources is that they can operate at room temperature without cryogenic coolers or bulky high vacuum systems, a feature that is highly desirable in many applications.

While signal sources for driving single channel receivers exist throughout the THz range, applications such as three dimensional (3D) Radio Detection and Ranging (RADAR) [14], Paper E, communication links [28], Nuclear Magnetic Resonance spectroscopy (NMR) [29], research setups and imaging systems, like the one featured in Paper D, call for an increasing amount of input power. Traditionally, this problem has been addressed either by increasing the number of devices used on the multiplier chip or by a waveguide-based power combination of several multipliers. However, today's high power Gallium Nitride (GaN) amplifiers operating in the millimetre wave region are providing more input power than traditional approaches can efficiently handle. The use of two dimensional (2D)-grid power combined frequency multipliers is a potential solution due to their high power handling capacity. In particular the first stage in a THz multiplier chain needs to handle high input powers, a fact that is illustrated in Figure 1.2. High power multipliers are needed when the frequency is too high to

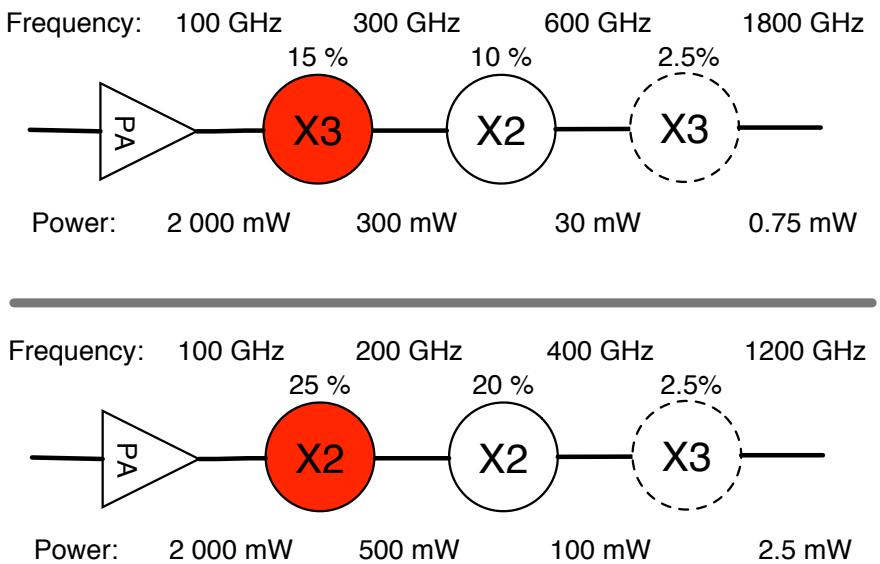

Figure 1.2: Schematic showing two examples of the power budget for cascaded frequency multipliers:2D grid power combined frequency multipliers may be an alternative for the first stages (red circle) in a high power THz source.

use amplifiers; today that breakpoint is at approximately 100 GHz. Combined with the recent advancements in GaN amplifier technology around 100 GHz, [30–32] , the settings are well suited to develop a high power frequency multiplier delivering record power levels at 200 GHz to 300 GHz.

The highest output power and efficiency among frequency multipliers used today is found in diode based passive designs; a summary of current state of the art performance can be found in Figure 1.1. Monolithic Microwave Integrated Circuit (MMIC) transistor technology has in recent years been making its way into the lower part of of the THz region [33]. However for the highest frequencies and highest power levels diode based multipliers still hold a dominant position. Most commonly used are Gallium Arsenide (GaAs) Schottky-diode multipliers and Indium Gallium Arsenide (InGaAs)/Indium Aluminum Arsenide (InAlAs) HBV-diode multipliers.

To achieve higher power levels in the traditional planar design of frequency multipliers two main routes exist. The first one is to add more diodes in series or parallel on the chip, a method that works well up to around 50 diodes [18, 34]. As the number of diodes increases, so does the loss and complexity in the matching network. The other path is to use a waveguide split and combine network to power combine many multiplier circuits [18, 35–38]. This method also works well for a small number of chips but as the number of circuits increase the split and combine losses becomes dominant. The use of planar grids offers an advantage for networks with many diodes (> 50), since the split and combine loss is independent of the number of devices [39]. Thus, the power handling capacity scales proportionally to the number of devices in the grid. A number of examples of free space operating 2D array frequency multipliers exist see e.g. [40–45]. Quasi-optical frequency multipliers with fewer active elements exist, see for example [46–48]. The downside of free space arrays is that the input and output coupling needs to be done quasi-optically using focusing elements, which leads to a bulky system. Waveguide embedded 2D grids are far less developed, [49, 50], Paper A and B, but offer a compact unit compatible with existing waveguide based systems. Waveguide embedded 2D grid multipliers promise high output power, efficient power combining of a large number of devices and reliability through graceful degradation [39, 51].

Chapter 2

Background of varactor grid frequency multipliers and THz imaging

The field of varactor frequency multipliers has a long heritage and detailed textbooks covering the topics were available as early as the 1960s, e.g. [52] by P. Penfield and R. P. Rafuse. The development of varactor frequency multipliers is still an active research topic and B.L Diamond's observation from 1963 still holds true;

> In the past few years the application of the semiconductor capacitor diode (varactor) to frequency multiplication has received considerable attention. B.L Diamond, 1963 [53]

Frequency multipliers at THz and millimetre wave frequencies can be realised in a great number of ways. This thesis will focus on two terminal semiconductor device based multipliers, with special emphasis on two designs based on HBV diodes [26] and Schottky diodes. In general, semiconductor diodes can operate as frequency multipliers either by modulation of the nonlinear bias dependent depletion region capacitance, under reverse bias, or by modulation of the non linear forward conduction, during forward bias. Varistor and varactor mode operation each dominate at the respective boundaries of the diode's bias region but a combination of the two nonlinear effects may be used as well.

The main advantage of a varactor frequency multiplier is the high conversion efficiency, in theory 100 % for a lossless varactor [54]. Resistive multipliers have the advantage of a less reactive matching network leading to a greater operating bandwidth [55] but suffer form an inherently lower conversion efficiency. The theoretical limit of conversion efficiency from a resistive multiplier is $1/n_{mult}^2$, where n_{mult} is the multiplication factor [56].

2.1 Varactor frequency multipliers

The simplest varactor model introduced in [57] and drawn in Figure 2.1 contains only a voltage dependent capacitance in series with a constant parasitic resistance. The key

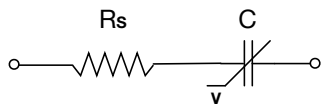

Figure 2.1: Uhlir's varactor model containing the voltage dependent capacitance in series with a parasitic resistance.

to varactor multiplier operation is that the capacitance of the diode varies with the applied voltage. When driven, commonly referred to as pumped, by a signal source of frequency f_p harmonics of the input frequency, $f_{n\times p}$, will be generated [58, 59]. An upper limit of the attainable performance of a varactor multiplier can be related to the dynamic cutoff frequency which relates the magnitude of the elastance modulation to the parasitic series resistance, R_s:

$$f_c = \frac{S_{max} - S_{min}}{2\pi R_s} \tag{2.1}$$

The dynamic cutoff frequency is a useful figure of merit when comparing varactor candidates for a multiplier design. It is also commonly used to evaluate tradeoffs when designing the epitaxial structure or layout of a varactor diode.

When using a single Schottky diode a voltage dependent differential elastance $S{=}1/C$, where C is the capacitance, curve of the "Schottky shape" in Figure 2.2 is obtained. For varactor operation the diode is direct current (DC)-biased somewhere in between the reverse breakdown voltage and forward conductance threshold, typically around $V_{BD}/2$. HBV diodes and other varactors with a symmetric elastance modulation function exhibit the behaviour illustrated by the "HBV line" in Figure 2.2 where the elastance is an even function around the zero bias point. If a varactor with an even elastance function and an odd conduction current function is operated around its point of symmetry only odd harmonics of the pump frequency will be generated.

The fundamental principle of varactor operation is that the width of the depletion region, and thus the capacitance can be changed by biasing the diode. To understand the origin of the capacitance modulation the physical construction of the devices need to be studied. HBV diodes utilises semiconductor heterojunctions to form a potential barrier. The devices are grown epitaxially with symmetric layers of moderately n-doped low band-gap materials (modulation layers) with an undoped high band gap material (barrier) sandwiched in between. The two heterojunctions connecting the barrier and the undoped barrier itself prevents electron transport through the epitaxial stack. Due

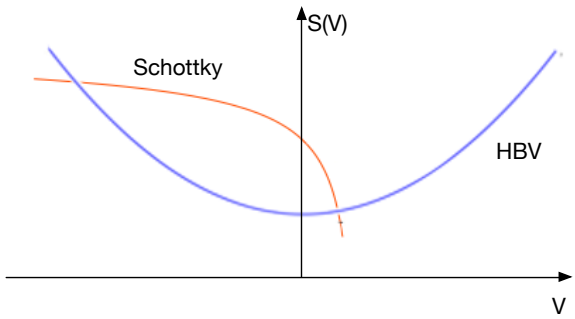

Figure 2.2: Typical differential elastance curves as a function of bias voltage for Schottky and HBV varactors.

to the symmetry and the epitaxial fabrication technique multiple layers can be stacked to increase the breakdown voltage of the structure. The epitaxial structure used in this work is outlined in Table 2.1. The spacers surrounding the barrier layers are added to stop dopants from the modulation layers from diffusing into the barrier during material growth. In the epitaxial stack presented the barrier height is improved through the addition of a thin pseudomorphic Aluminum Arsenide (AlAs) layer in the centre of the barrier [60].

Table 2.1: The epitaxial structure of the HBV diodes used in this work. For the three barrier devices used the layer sequence 3 to 8 is repeated three times.

Rep	No	Layer	Thickness (nm)	Material	Doping (cm^{-3})
	22	Contact	400	$In_{0.53}Ga_{0.47}As$	$> 10^{19}$
	21	Modulation	250	$In_{0.53}Ga_{0.47}As$	10^{17} (N_{dop})
	...	...	...	...	...
x3	8	Spacer	5	$In_{0.53}Ga_{0.47}As$	Undoped
x3	7	Barrier	5	$In_{0.52}Ga_{0.48}As$	Undoped
x3	6	Barrier	3	AlAs	Undoped
x3	5	Barrier	5	$In_{0.52}Ga_{0.48}As$	Undoped
x3	4	Spacer	5	$In_{0.53}Ga_{0.47}As$	Undoped
x3	3	Modulation	250	$In_{0.53}Ga_{0.47}As$	10^{17} (N_{dop})
	2	Buffer	1000	$In_{0.53}Ga_{0.47}As$	$> 10^{19}$
	1	Spacer	100	$In_{0.53}Ga_{0.47}As$	Undoped
	0	Substrate	InP		SI

For the general understanding of the device physics the barrier can be assumed to be

homogeneous, the conduction band diagram of such device is sketched in Figure 2.3 (a). The barrier can be viewed as the plate separation in a parallel plate capacitor. When the HBV is biased, Figure 2.3 (c) the modulation layer of one side of the barrier will be depleted, effectively widening the charge free region, therefore decreasing the junction capacitance. The differential capacitance of an HBV diode can be calculated as

$$C_{HBV}(V) = \frac{A}{N} \frac{1}{\frac{b}{\varepsilon_b} + \frac{s}{\varepsilon_d} + \frac{w}{\varepsilon_d}} \tag{2.2}$$

$$w = \sqrt{\frac{2\varepsilon_d |V_d|}{qN_d}} \tag{2.3}$$

where A is the device area, N is the number of barriers, b is the barrier thickness, s is the spacer thickness, w the depletion layer width, ε_d and ε_b is the permittivity of the depletion layer and barrier respectively, V_d is the bias voltage, C_{max} is the doping concentration in the modulation layer and q is the elementary charge. The model is valid as long as the breakdown field in the semiconductor is not exceeded or the depletion layer does not punch through the full modulation layer. However, to calculate the maximum capacitance occurring at zero bias charge screening effects need to be included, C_{max} is therefore given by

$$C_{max} = \frac{A}{N} \frac{1}{\frac{b}{\varepsilon_b} + \frac{2s}{\varepsilon_d} + \frac{2L_D}{\varepsilon_d}} \tag{2.4}$$

$$L_D = \sqrt{\frac{kT\varepsilon_d}{q^2 N_d}} \tag{2.5}$$

where L_d is the Debye length, k is Boltzmann's constant and T is the device temperature.

A Schottky diode is made by bringing a metal into contact with a semiconductor [61]. When the metal comes into contact with the semiconductor the fermi energy level of the semiconductor will align with that of the metal and thus produce a potential barrier. This is illustrated in Figure 2.3 (b), where the conduction band of a n-type Schottky diode is sketched. In order to align the fermi levels electrons need to flow from the semiconductor to the metal to create a electrostatic potential, compensating for the original difference in fermi levels. It is this net charge of electrons that create the potential barrier and at the same time the electron vacancies in the semiconductor will create an area with a positive net charge. The width of this electron depleted region, denoted w in Figure 2.3, can be changed by biasing the varactor. Similarly as for the HBV diode the junction capacitance of a Schottky diode is bias dependent through modulation of the depletion layer thickness:

$$C_{Schottky}(V_d) = \frac{\varepsilon_d A}{w(V_d)} = A\sqrt{\frac{q\varepsilon_d N_D}{2\left[\psi_{bi} - (kT/q) - V_d\right)]}} \tag{2.6}$$

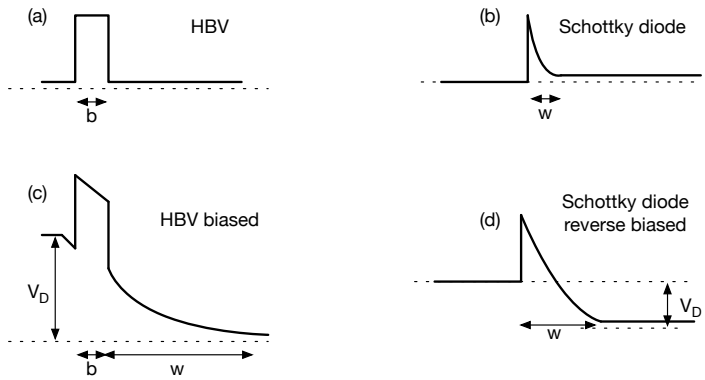

Figure 2.3: Conduction band diagram for an unbiased HBV diode (a), an unbiased Schottky diode (b), a biased HBV diode (c) and a reverse biased Schottky diode (d).

for bias voltages ranging to from the $\psi_{bi}/2$ to the reverse breakdown voltage, where ψ_{bi} is the built in potential of the Schottky contact.

As the design work proceeds more and more elements are usually added to the model to improve the accuracy of the simulation. The shape of a varactor's capacitance curve is directly coupled to the semiconductor design used and varactor optimisation is a topic in itself [62]. In [63] the effect of the shape of the elastance curve, coupled to different epitaxial structures, upon multiplier efficiency for symmetric varactors was investigated.

2.1.1 Varactors modelling

Even though the ideal varactor models in Figure 2.1 serve as a good starting point for a multiplier design, parasitic effects needs to be included to accurately predict the performance of a THz frequency multiplier. A more elaborate varactor diode model is presented in Figure 2.4. It includes the voltage dependent capacitance, the voltage and temperature dependent conduction current, and two parasitic elements. A good approximation for the charge dependent voltage over the particular HBV diode used in this work is the cubic varactor model, Equation (2.7), suggested by [64].

$$V_{HBV}(Q) = S_{min}Q + (S_{max} - S_{min})(\beta\frac{Q^3}{Q_{max}^2}) \tag{2.7}$$

Where V_{HBV} is the voltage across the varactor as a function of the stored charge Q. S_{max} and S_{min} the varactor's maximum and minimum elastance, q_{max} the maximum

charge and β a fitting parameter. For more accurate Harmonic Balance simulations the charge dependent voltage is usually calculated by the quasi-static HBV model

$$V_{HBV}(Q) = N\left(\frac{bQ}{\varepsilon_b A} + \frac{sQ}{\varepsilon_d A} + sign(Q)\left(\frac{Q^2}{2qN_d\varepsilon_d A^2} + \frac{4kT}{q}\left(1 - e^{-|Q|/(2L_d AeN_d)}\right)\right)\right) \tag{2.8}$$

where L_d is the Debye length from Equation (2.5) [65]. The semi physical model is useful due to the coupling to device parameters. For temperatures up to approximately room temperature thermionic emission is the dominant current transport mechanism in the HBVs used in this work [66]. The following empirical model is used for simulations:

$$I_b(E_b) = A \cdot a \cdot T^2 \cdot Sinh\left(\frac{E_b}{E_0}\right) e^{-\frac{\phi_b}{kT}} \tag{2.9}$$

The electric field in the barrier E_b can be calculate by applying Gauss' Law, $Q = E_b\varepsilon_d$, to Equation (2.8). E_0, a, and ϕ_b are fitting parameters that need to be extracted from measurements.

A good approximation of the junction capacitance of a uniformly doped Schottky diode can be derived from Equation (2.6) if the thermal voltage $V_t = kT/q$ is neglected [67]:

$$C_{Schottky}(V_d) \approx \frac{C_{j0}}{\sqrt{1 - \frac{V_d}{\psi_{bi}}}} \tag{2.10}$$

where C_{j0} is the zero bias junction capacitance. Current transport in n-type Schottky diodes is dominated by electron majority carriers. For the high mobility GaAs Schottky diodes in this work thermionic emission over the barrier is the major transport mechanism followed by quantum mechanical tunnelling through the barrier. These two processes are described in [68]. A widely used model combining these two effects is:

$$I(V_d) \approx I_0\left(e^{\frac{qV_b(V_d)}{\eta kT}} - 1\right) \tag{2.11}$$

$$V_b(V_d) = V_d - R_s * I \tag{2.12}$$

where I_0 is the saturation current that is obtained from measurements by extrapolating a log-linear plot to $V_d = 0$, η is the ideality factor that is $\eta \approx 1$ if the tunnelling current can be neglected, I it the current through the diode and R_s is the series resistance [61].

The parasitic series resistance in both HBV and Schottky diodes has three main contributions:

- Bulk resistivity in the modulation layers, where the extension of the depletion region is voltage dependent, and the buried contact/buffer layer.
- Contact resistance.
- Ohmic losses in the connecting air-bridges which are frequency dependent due to the skin effect.

The parasitic series inductance for originates mainly from the air-bridges, see Figure 2.5 for the geometry of a typical planar HBV diode.

At high frequencies and high powers the finite electron velocity in the semiconductor material will influence the performance through current saturation effects [69]. High power levels will also increase the conduction current, acting as a parasitic varistor in parallel with the varactor. If the drive level exceeds the varactor's reverse breakdown voltage the conduction current will increase rapidly leading to an effective decrease in conversion efficiency, since resistive harmonic generation is far less effective than reactive. Another problem with high power levels is the self heating of the diode which also degrades performance [70].

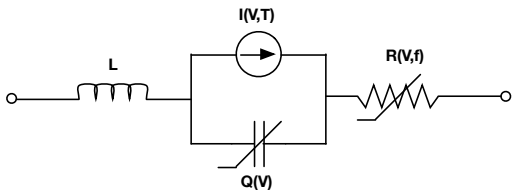

Figure 2.4: A varactor model including a voltage and temperature dependent conduction current, voltage and frequency dependent series resistance along with a parasitic inductance.

2.1.2 Varactor multiplier matching

By optimising the source and load impedances at the input and desired harmonic frequency a large portion of the input power can be converted to the output frequency, ideally 100% for a lossless varactor without parasitic elements. The source and load impedances are generated by filter structures at the in and output, see Figure 2.6 for a two-port transmission line representation of a single HBV diode frequency multiplier. Since both input and output circuits interact, the impedances in a final design are often based on a number of compromises; typically the impedance presented to the varactor at the input frequency has a greater effect on final performance. Besides the pump frequency and the desired output harmonic it may be necessary to terminate other harmonics with suitable impedances, referred to as *idler circuits* [53]. An example would be if a single non-symmetric varactor is to be used as a frequency tripler the second harmonic idler and possibly also the fourth harmonic idler would need to be terminated with proper idler circuits. Similarly for an HBV diode operating as a quintupler, where the performance is greatly improved if the third harmonic is terminated in a reactive idler circuit [63].

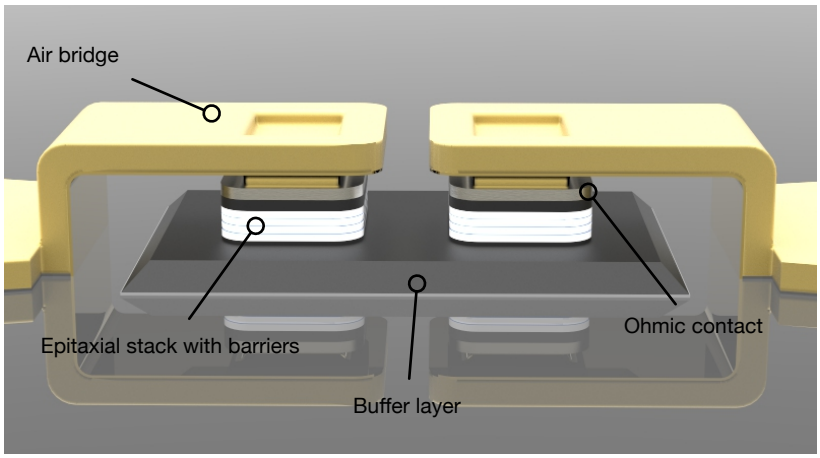

Figure 2.5: Picture showing a typical HBV diode consisting of two three-barrier mesa stacks contacted by air bridges at the top and a buried buffer layer in-between at the bottom.

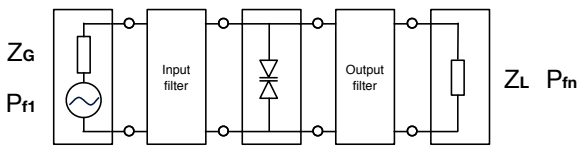

Figure 2.6: Two port models of a shunt mounted HBV diode together with input and output filters. The pump frequency is injected through the source at the left side and the power generated at the desired harmonic frequency is absorbed in the load at the output.

2.2 Grid frequency multipliers

Quasi-optically coupled frequency multipliers, e.g. [71], have existed before quasi-optical power combining of microwave devices became a research topic [72]. The naming convention within the field is somewhat confusing, the terms quasi-optical power combining, grid power combining, 2D-grid power combining, array power combining or even grid array power combining are sometimes used interchangeably. Systems coupled together by the optics and free space propagating waves are more often referred to as quasi-optical and arrays, while waveguide embedded structures more often are called grids. See Figure 2.7 and Figure 2.8 for examples of the concepts. Most frequency multiplier grids presented so far have been designed for free space operation, sometimes also referred to as open structures, where the input and output signals are coupled to

the circuit quasi-optically. This is done by either illuminating the array in the far field of an antenna where the incident field can be well approximated by a plane wave. Or by using focusing optics and thereby provide a Gaussian shaped power density across the target array. The modelling of free-space arrays is more developed than for the waveguide embedded arrays and experimental data exists to verify, cf. [73–75]. However many experiments with free space arrays have been performed by illuminating the array in the far field of a high power source e.g a free-electron laser. By doing so the plane wave illumination condition assumed in the unit cell modelling is fulfilled but only a small fraction of the pump source output power couples to the the array, so even though the array conversion efficiency is quite good the overall system efficiency is very low. It is generally hard to provide an even illumination without suffering from large spillover losses. Also, the downside of free space arrays is that the total setup becomes bulky and less flexible compared to a waveguide packaged component. In addition, the electronics community is used to standardised waveguide interfaces between components, rendering open quasi optical solutions impractical for applied system design. A summary of relevant grid frequency multipliers is given in Table 2.2.

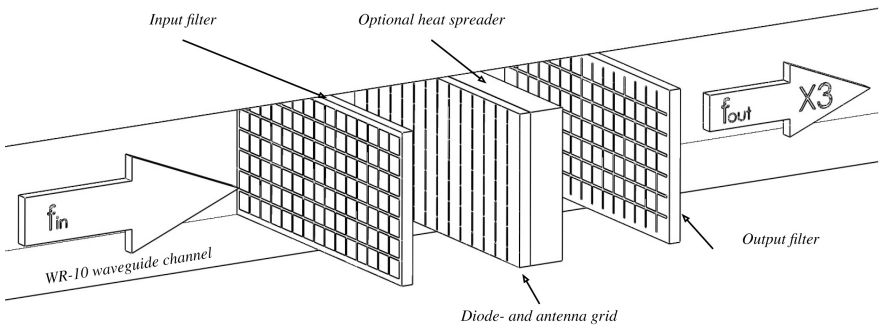

Figure 2.7: A conceptual sketch of a waveguide enclosed grid frequency multiplier.

One of the main motivations for building 2D arrays of frequency multipliers is to increase the power handling capacity of the assembled frequency multiplier. The traditional circuit design methods struggle when the number of diodes in the multiplier circuit becomes too many to easily match the multiplier, this typically happens between ten and fifty diodes. In a grid of frequency multipliers an arbitrary grid size of m x n frequency multipliers can be chosen without affecting the power combining loss, however the advantage in terms of power handling compared to traditional power combined designs increases as the total number of devices increases [39].

As mentioned above, one of the advantages of packaging grids in waveguides is that it enables integration into systems by means of standardised waveguide interfaces, operating with the H_{10} mode. This also makes characterisation of the components easier since calorimetric power meters can be coupled to the waveguide interface thus

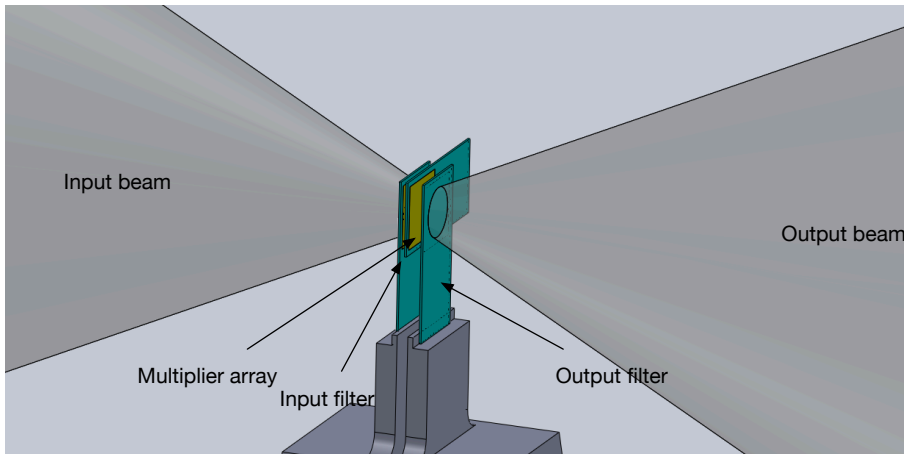

Figure 2.8: A conceptual sketch of a free space array frequency multiplier.

eliminating the need to estimate optical coupling losses. However, when packaging an array in a waveguide the uniform plane wave excitation assumed in unit cell modelling does not hold true. In a fundamental mode H10 waveguide mode, also known as TE10 (H10) waveguide the e-field varies as $\sin(x)$, and the power density as $\sin^2(x)$, with a constant phase along the broad waveguide dimension. The work in this thesis and previous work within the field, [49, 50], are using a fundamental mode waveguide at the input frequency which then becomes over-moded at the desired harmonic. The uneven power distribution means that the elements of a symmetric uniform array will receive different input powers depending on their position in the array, an issue that is further discussed in Section 3.2.

2.3 Imaging applications

Millimetre wave and THz imaging has been applied in a large number of applications including biology and medicine [78–85], non invasive imaging [12, 13] and security screening [16, 17, 86]. There are three main reason for the interest in applying THz and millimetre waves in imaging applications. Most dielectric materials are transparent in this frequency range making common packaging materials and clothing transparent, a fact that is utilised in security screening applications. Polar molecules e.g water show strong absorption due to vibrational and rotational modes resonating with the wave, which makes sample investigation systems very sensitive to differences in water content. The wavelength range 1 mm to 0.1 mm offers a reasonable resolution given the two mentioned advantages.

Table 2.2: Summary of relevant grid frequency multipliers presented to date. X2 represents a frequency doubler and X3 a frequency tripler.

Type	Output	Eff. @ P_{max}	Nr. devices	Ref
X3 abrupt varactors[q]	40 mW @ 15 GHz	14 %	16	[73]
X2 Schottky[f p]	500 mW @ 66 GHz	10 %	760	[75]
X2 BNN [f p]	2.1 W @ 66 GHz	7.5 %	1760	[74]
X3 SQBV[f p]	5 W @ 66 GHz	2 %	3100	[76]
X2 Schottky[q]	100 μW@ 290 GHz	0.14 %	7	[77]
X2 Schottky[q]	24 mW @ 1 THz	0.05 %	144	[44]
X3 MQBV[w p]	148 mW @ 90 GHz	1.8 %	260[a]	[50]
X2 Schottky[w p]	410 mW @ 65.8 GHz	5 %	98[a]	[50]
X3 HBV[w]	684 mW @ 93 GHz	10 %	196	[49]
X3 HBV[w]	35 mW @ 247 GHz	3.9 %	72	A
X2 Schottky[w]	0.25 W @ 183 GHz	19 %	128	B

[a] Estimation from available information
[f] Far field measurement with a plane wave excitation
[p] Pulsed measurement
[q] Quasi-optical focused measurement system
[w] Waveguide enclosed

For sample investigation at close range the transmission or reflection properties are often of interest, as in the example in Paper D. The properties of the sample are then calculated from the perturbation of the amplitude and phase of the incident field and reconstruction algorithms are often used. Stand-off imaging used for such applications as security screening and packet inspection often use Frequency Modulated Continuous Wave (FMCW) radars for the image acquisition. An FMCW radar transmits a frequency sweep and determines the down-range distance to the target by the mixing product of the transmitted and received signal. The intermediate frequency revealing the range is given by

$$f_{IF} = \frac{2KR}{c} \tag{2.13}$$

where K (Hz/s) is the chirp rate, R (m) the target range and c (m/s) the speed of light. The theoretical limit for the down range resolution is determined by the sweep bandwidth as

$$\Delta_r = \frac{c}{2\Delta_f} \tag{2.14}$$

where Δ_f (Hz) is the chirp bandwidth [87]. The high bandwidth achievable in the lower THz region combined with atmospheric absorption windows makes these systems attractive. The cross range resolution is limited by diffraction, thus it is coupled to the size of the main reflector in the optical focusing system.

Different approaches exist to couple the transmitted radio frequency (RF) signal into the optics and extracting the reflected signal to the receiver. In Figure 2.9 two common approaches are shown. The first one uses a beamsplitter to enable physical separation of the transmitter and receiver module. This is needed since the optics only has one focal point on the electronic side of the system without the beamsplitter. The second approach uses a transceiver module like the one presented in Paper E. Since the transmitted signal (Tx) and received signal (Rx) share the same antenna feed and polarisation only one focused point is needed in the system. More advanced schemes also exists one being an approach where an orthomode transducer (OMT) is used to combine the Tx and Rx signals to the same antenna feed but with orthogonal linear polarisations. A reflecting grating polariser converter then converts the Tx signal from linear to circular polarisation. When the circularly polarised radar beam reflects on the target the rotation will turn. Thus, when the reflected signal reaches the grating polariser it will convert into the linear polarisation of the receiver [87].

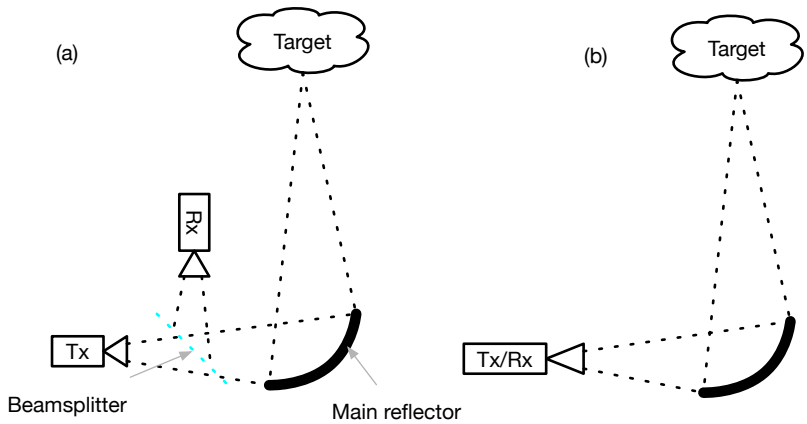

Figure 2.9: Two different stand off imaging system setups. a) Uses a beamsplitter to combine the Tx and Rx beam paths. b) Uses a transceiver module where the Tx and Rx channel has the same polarisation from the feed.

Chapter 3

Modelling and design of waveguide enclosed frequency multiplier grids

This chapter provides an overview of the modelling approaches used in this work. The first part outlines the cascaded unit cell approach that was used for initial design of the grid presented in Paper A. This is then followed by a description of how several sets of cascaded unit cells can be paralleled to account for the excitation present in waveguide enclosed 2D-grids. Paralleled sets of cascaded unit cells were successfully applied in the design of the frequency doubler in Paper B. The two mentioned approaches are useful during the design process due to their low computational cost, thereby enabling fast iterations. The down side of unit cell modelling is the symmetries assumed which makes the model fully valid only for infinite grids with plane wave excitation. To account for these effects a full 3D modelling approach was developed in Paper C. This model is useful for design verification and advanced failure and yield modelling. Altogether these three modelling approaches provides an attractive method for the design of waveguide enclosed grid frequency multipliers.

The end of this chapter provides complementary information about the design of the frequency multipliers in Paper A and B. Furthermore the concept of using a shim system for the mounting of the frequency multipliers is explained and exemplified by an in-depth description of the shims used in Paper B. Important aspects of mechanics design for millimetre and THz electronics are also discussed. Finally the matching network used for free space tests of the HBV frequency tripler grid is described.

3.1 Cascaded unit cells

The most common approach when designing large grids of identical elements is to model the device using the unit cell approach. When doing so, periodic electric and magnetic boundary conditions are enforced on the borders of the symmetric cells, assuming an infinite array of identical elements operating in phase. In this way the computational burden can be reduced to solving a single cell. In reality no grids are infinite in size but the method has proven useful even for relatively small grids.

Simpler unit cell structures can with good accuracy be approximated using the induced electromagnetic force (EMF) method, described in [88, 89], which is a development of the work by Eisenhart and Khan [90]. This approach has the advantage that a lumped element model with analytical expressions relating to the the unit cell dimensions can be created. For the initial design work this can be a very useful tool to find a good starting point for more precise 3D electro magnetical (EM) simulations, that later can replace the EMF model. For more complex geometries where the basic assumptions in the EMF method become too complex, a full wave commercial 3D EM field solver may be used directly to create the unit cell model.

A grid multiplier array usually consists of a number of components that can be approximated using the unit cell approach, such as the input filter, the active array and the output filter. It was shown in [91] that several grids containing unit cell models could be cascaded using transmission line theory [92]. By applying that approach, well known transmission line techniques can be applied when designing the input and output matching networks. As an example a plate with a predetermined thickness that is inserted in the path of the propagating wave will act as a transmission line with a wave impedance determined by the permittivity, assuming lossless and nonmagnetic materials, of the material and electrical length determined by the thickness.

Care must be taken when modelling cascaded grids since the model does not include evanescent coupling between the grids, this effect is further described in Section 3.4 and Paper C. In practice this means for example that two metallic filter surfaces cannot be modelled separately and then be put into the transmission line model right next to each other, since the evanescent field coupling that occurs between the filters is not included in the transmission line model. Metallic patterns such as antennae and filters must also be modelled with the correct dielectric backing, which later can be de-embedded, in order to correctly account for the added capacitance in gaps, for instance.

The cascaded unit cell modelling approach enables the use of different sized unit cells in cascade and individual elements can be represented either by approximate lumped component models or by more exact numerical simulation files. The thickness of substrates and air-gaps can also easily be used as tuning parameters in the model; an example of a typical transmission line model of a grid multiplier being shown in Figure 3.1. The model in Figure 3.1 is usually solved using a Harmonic Balance simulator to evaluate the expected frequency multiplier performance.

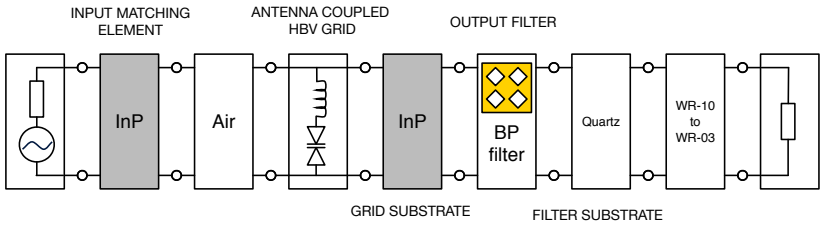

Figure 3.1: An example of a complete multiplier setup as a transmission line model for harmonic balance simulations.

3.2 Grids enclosed in a waveguide cavity

One of the main practical differences when using the unit cell approach to model grids in waveguides compared to TEM environments is that the wave impedance seen on the two plane wave ports is frequency dependent while in a free space environment only the electrical phase length is frequency dependent. The wave impedance of the H_{10} mode in a rectangular waveguide is known to be [93, 94]:

$$Z_{H_{10}} = \frac{Z_0}{\sqrt{1 - \left(\frac{f_c}{f}\right)^2}} \tag{3.1}$$

Where f_c is the cutoff frequency for the mode, f is the frequency and

$$Z_0 = \sqrt{\frac{\mu_0}{\varepsilon_0}} \approx 377\Omega \tag{3.2}$$

is the characteristic impedance in vacuum. From Equation (3.1) it is clear that as the frequency increases the wave impedance in the waveguide will approach that of a free space propagating wave. It also means that for a grid multiplier in a waveguide environment the fundamental frequency and the generated harmonic frequency will experience different wave impedances. The impedance difference between the fundamental frequency and the harmonic frequency will be less if the wave propagates through, for example, a dielectric matching plate with high permitivity.

3.3 Paralleled sets of cascaded unit cells

The grid multipliers presented in this thesis are both placed in a rectangular waveguide with a H_{10} input and output mode. As a consequence the unit cells in the grid will be

pumped with different input powers. In order to model this effect a modelling approach with paralleled sets of cascaded unit cells was developed. Since the columns of the grid are aligned with the E-field of the H_{10} input mode the input power is assumed to be constant among the cells in a column. As a first approximation of the input power to each cell a relative power density was calculated based on the cross section area occupied by each unit cell and the H_{10} mode power density. On the input side the pump power for a unit cell in column col_n is calculated as

$$P_{cell}(col_n) = \frac{P_{AVA}}{m} \cdot \frac{\int_{col_n - 1 \cdot \pi/n}^{col_n \cdot \pi/n} sin^2(x)\ dx}{\int_0^{\pi} sin^2(x)\ dx} \tag{3.3}$$

where col_n is the number of the column, P_{AVA} is the total available power, m is the number or rows in the grid and n the number of columns in the grid. The input phase is assumed to be equal to all unit cells. Simulations presented in Paper C validates that the two above assumptions are a good approximation for the input power.

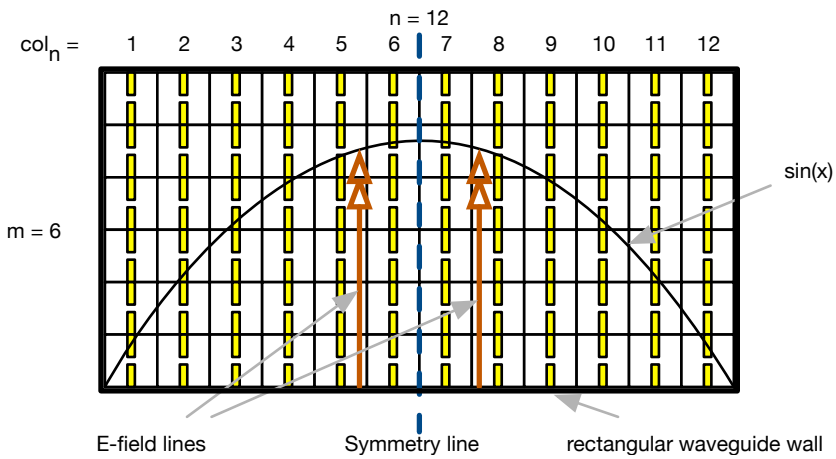

Figure 3.2: A schematic of six by twelve unit cells in a rectangular waveguide. The E-field distribution and two lines indicating the field orientation of the H10 mode are also plotted. The numbering scheme used to calculate the input power is also displayed.

To account for the difference in conversion efficiency and output phase a set of equal chains of cascaded unit cells are simulated with input powers according to the above assumptions. The outputs from the different sets are then coupled to a common load by power combiners in the simulation software, thus their relative phases are accounted for; a schematic of the setup is drawn in Figure 3.3. A further simplification used is the electrical symmetry line drawn in Figure 3.2, whereby only half of the columns need to be included. In total one cell from each column on either side of the symmetry line is simulated, which is illustrated in Figure 3.3. In this way both the difference in

conversion efficiency caused by the varying input power and the difference in output phase caused by the input power dependent average capacitance are accounted for. The passive embedding network is equal for all the unit cells and it is assumed that the output H10 mode must have an equal phase plane at the grid surface similar to the input mode. In Paper A this method is denoted vector summed efficiency. The same paper also describes an alternative summation denoted scalar summed efficiency where the output powers from the unit cell sets are simply summed. The scalar summed efficiency is thus calculated as:

$$Efficiency_{scalar} = \frac{\sum_1^n P_{out,unit\ \ cell\ col\ n} \cdot m}{P_{AVA}} \cdot 100 \tag{3.4}$$

where $P_{out,unit\ \ cell\ col\ n}$ is the output power from a unit cell in column n. The difference between these two methods shows that the output phase plays an important role in coupling to the output mode.

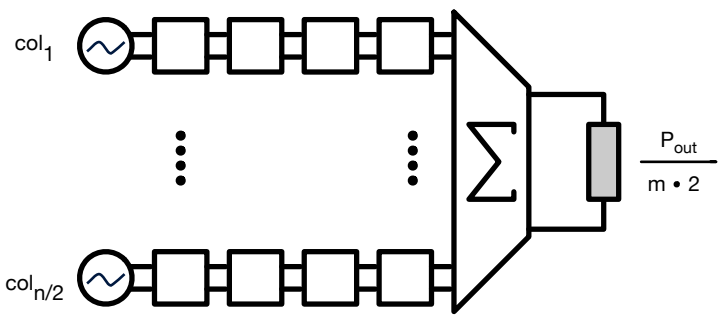

Figure 3.3: A schematic illustration of paralleled sets of cascaded unit cells. Each set of cascaded unit cells is driven with the input power calculated above. The outputs are the summed using either the scalar or vector approach. Note that only one unit cell from half of the columns are simulated due to the assumed symmetries.

3.4 Full 3D modelling with a large number of nonlinear devices

The two modelling methods presented above are both computationally effective and therefore suitable for the iterative work of designing a frequency multiplier. Papers A and B confirm that good results can be achieved with the presented methods but

also that more work is needed. Even though the conversion efficiency simulation followed the measured data well at the peak output power the frequency response showed a resonant behaviour and the envelope of the output power was slightly shifted down in frequency. There are many potential sources of these discrepancies that the unit cell models are unable to detect, examples being substrate modes, near field coupling between the grids and higher order mode excitations caused by the mounting pockets.

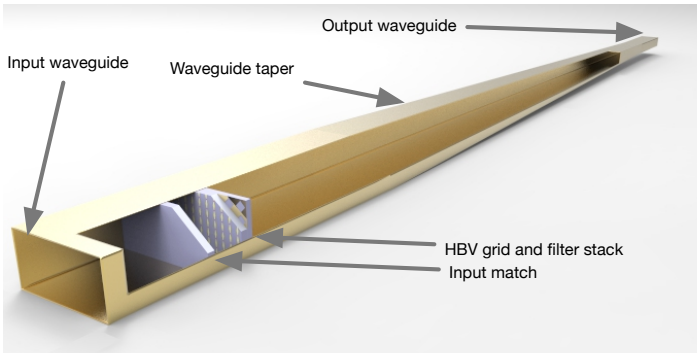

Figure 3.4: Full 3D simulation model volume, the complete waveguide cavity and all diode ports are included in the simulation. part of the waveguide has been removed to show the internal parts

Therefore a full 3D model was developed in Paper C for the design in Paper A. In the full 3D model the complete linear electromagnetic environment is simulated in a finite element frequency domain solver. Ports are placed in the simulation model at the waveguide input and output and at all diode positions. The s-parameter matrix is then imported to Harmonic Balance simulation software and a model with non linear-devices attached to all diode ports is created. A schematic of this simulation model is shown in Figure 3.4.

Paper C showed that this approach better predicted the response as a function of frequency than the unit cell models. In Figure 3.5 and Figure 3.6 field plots from the model is shown. In order to generate the plots the full 3D problem was solved according to the above description, using the quasi static HBV model from Equation (2.8). The current and voltages on the varactor ports in the harmonic balance simulation were then imported to the 3D EM solver as as excitation sources and the resulting fields were plotted on the mesh. The input tone behaves as expected, only a small fraction of the power passes the bandpass filter and reflects on the taper. If the phase of propagating third harmonic is changed a standing wav pattern can be noticed on the output. This is interpreted as higher order modes reflecting off the taper.

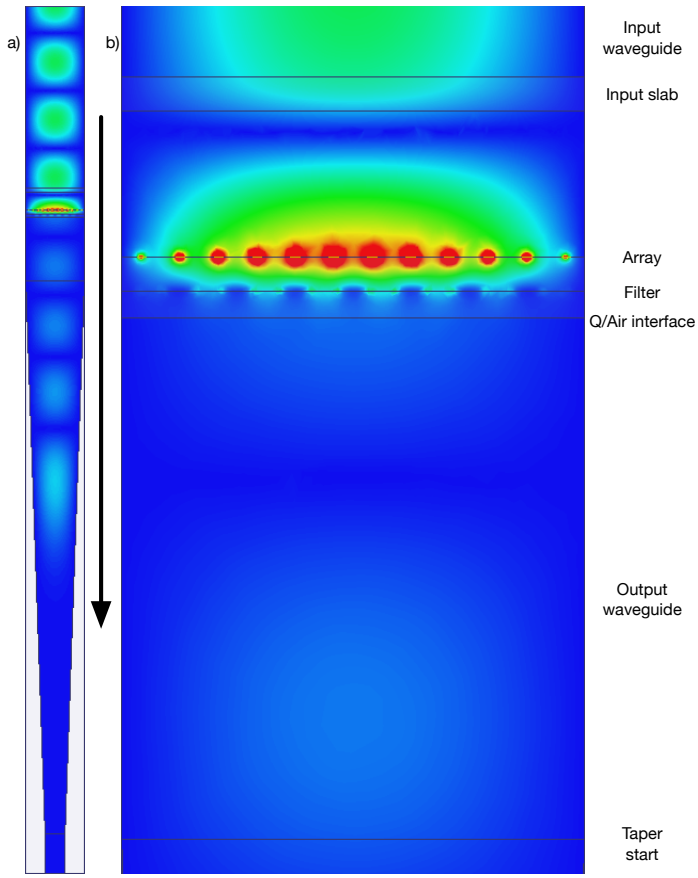

Figure 3.5: Example of field plots from the full 3D simulation, the input tone is plotted a) A cut through the entire simulation volume from above. b) Plot from the same view of the area next to the HBV grid. The arrow indicates the direction of signal propagation. From the data generated for Paper C.

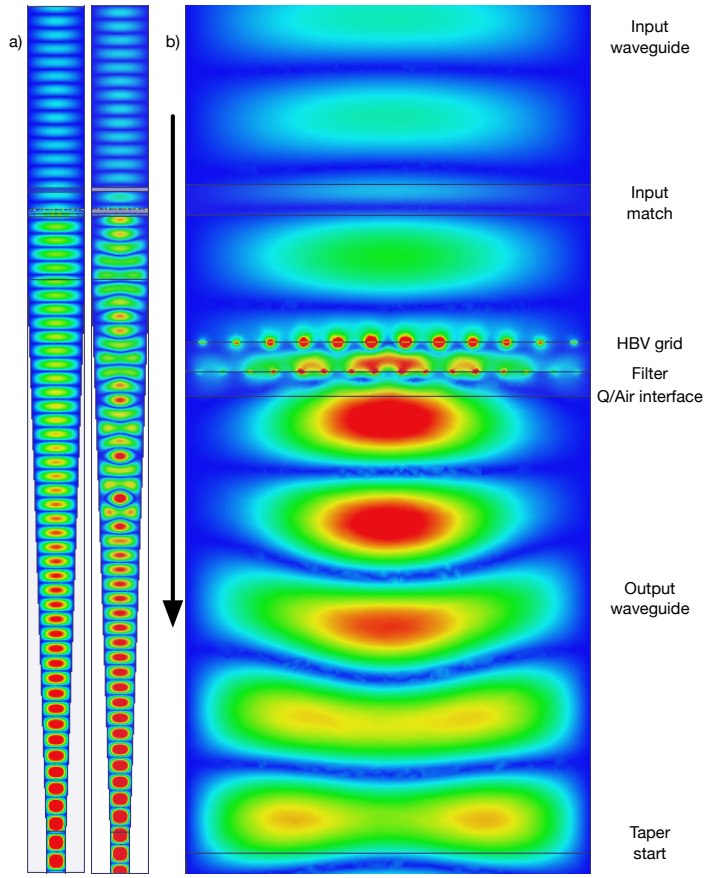

Figure 3.6: Example of field plots from the full 3D simulation, the output third harmonic is plotted a) A cut through the entire simulation volume from above, in two versions with different phase of the propagating wave. This reveals what seems to be higher order modes reflecting off the taper. b) Plot from the same view of the area next to the HBV grid. The arrow indicates the direction of the desired signal propagation, some of the third harmonic power is propagating towards the input. From the data generated for Paper C.

3.5 Design of a 249 GHz HBV frequency tripler grid

The design of any type of frequency multiplier is an iterative process. Many interactions exist between different design parameters and a number of tradeoffs need to be balanced against each other. Typical input parameters for a design may include input and output frequency, bandwidth, output power and conversion efficiency. In this design, presented in Paper A, HBV diodes based on the epi-stack design from [95] were used. It was also desirable to build an array that could be tested both in free space operation as well as in a waveguide cavity, the motivation for this being to gain experience in both types of design.

The unit cell size chosen for this design is 211 μm which gives a 12 by 6 element 2D grid if mounted in a standard WR-10 waveguide. A WR-10 waveguide was chosen on the input side since this meant that no additional input waveguide taper had to be manufactured, which made testing easier.

The compromise in the waveguide case was to use a unit cell large enough to receive sufficient power for efficient varactor frequency multiplication but at the same time small enough not to excite higher order modes. Given the unit cell dimensions and the available input power an HBV varactor optimised to operate with 20 mW input power at 83 GHz was designed. With the epitaxial material used this resulted in the 30 μm^2, two mesa, six barrier HBV varactor shown in Figure 2.5.

A dipole-like antenna structure was chosen for the antenna array after many iterations between a Finite Element Frequency Domain solver, used to simulate the unit cell, and a Harmonic Balance circuit solver, used to simulate the entire multiplier circuit. A lumped element model of the unit cell was produced using the induced EMF method, and both models can be seen in Figure 3.7.

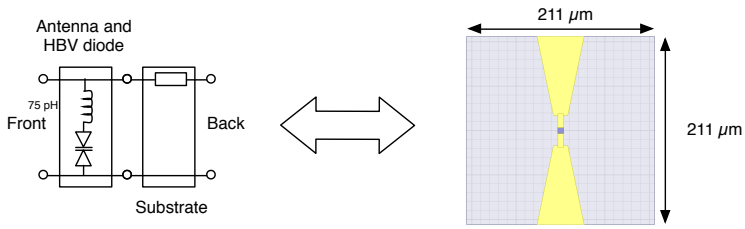

Figure 3.7: An analytical two-port transmission line model, from the induced EMF method, together with the equivalent unit cell used for FEM modelling. The yellow part of the unit-cell represents the antenna metal structure, where the HBV varactor is positioned in the centre.

The module's simulated scalar- and vector conversion efficiencies are plotted in Figure 3.8 together with the simulated conversion efficiencies for the individual columns.

Column numbering starts from the central symmetry line and moves out towards the edge, an illustration can be found in Paper A, Figure 3.

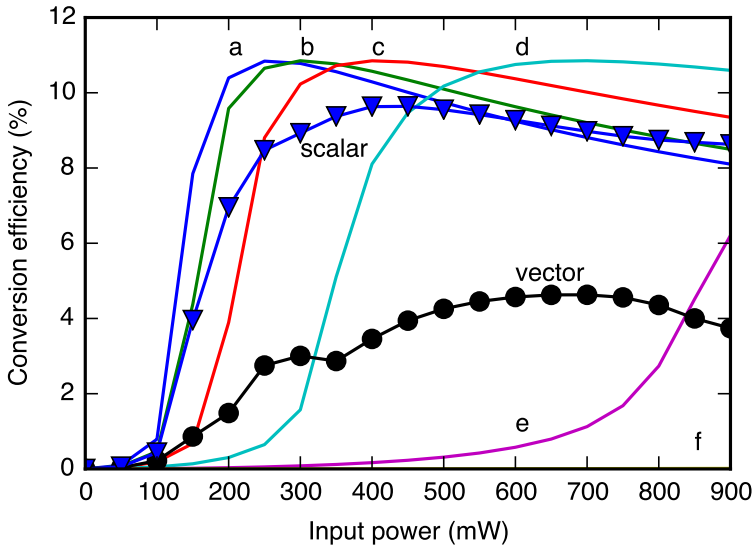

Figure 3.8: Simulated conversion efficiency for the six columns as a function of input power, for which column f is not visible due to a conversion efficiency close to zero. The calculated vector summed efficiency and scalar summed efficiency are also plotted. All data are for 247 GHz output frequency with the design tuned for 500 mW of input power.

3.5.1 Filters and matching elements for waveguide cavity operation

To realise the embedding network needed for optimum frequency multiplier operation a combination of dielectric matching slabs and a bandpass filter was used. Since both the input frequency and the third harmonic propagate in the same environment all matching elements except the last quartz slab at the output affect the varactor embedding impedance on both harmonics. It can therefore be hard to separate the effect of the different components in the matching network, presented in Figure 3.9, but some general properties will be outlined.

Starting from the input side of the multiplier a piece of InP substrate is used to match the input signal and thereby maximise the power transfer to the diodes. To create the filter needed for efficient multiplier operation a dielectric backed metal surface with a periodic metal pattern was used, commonly referred to as a frequency selective surface. The design of frequency selective surfaces, or filters, is well covered in

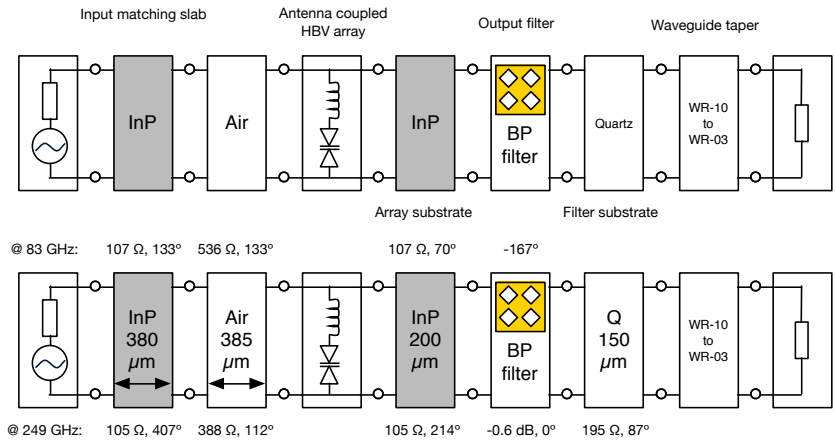

Figure 3.9: A complete unit cell transmission line model of the frequency tripler 2D array. The schematic at the top describes the functional blocks and the bottom version of the same circuit provides details about the electrical properties.

	Wave impedance [Ω]		
Material	83 GHz	249 GHz	Free space
Air	536	388	377
InP	109	107	105
Quartz	208	195	193

Table 3.1: H_{10} wave impedance in a WR-10 waveguide filled with a dielectric at the two critical frequencies in the design and complementary data for a free space propagating wave.

the literature [96]. An important aspect when designing a filter is to consider the wave impedances on both sides, which depend on whether a dielectric support substrate is used or not. A summary of the wave impedances in a WR-10, H_{10} waveguide environment for the materials used is given in Table 3.1 for reference. The filter resonant frequencies will also be affected by the surrounding wave impedances, i.e. the resonant frequency for a planar periodic filter mounted in a H_{10} mode waveguide will differ from the same filter resonant frequency in free space operation. The design used here employs a Rhombic aperture bandpass filter fabricated on a quartz substrate at the output to pass the third harmonic and reflect the first harmonic. The output filter together with the multiplier grid substrate serves many purposes, see Figure 3.10, namely:

- Acts as a back-short at the input frequency; The substrate roundtrip phase plus the reflection phase of the filter at f_1 should add to 0 (or $n \times 2\pi$).
- Matches the output frequency, f_3, with minimum loss.
- Transfers the propagating f_3 to the output waveguide impedance; the quartz substrate acts as a $\lambda/4$ transformer between the InP array substrate and the air filled WR-10 waveguide.
- Transfers heat from the array to the metal waveguide block.

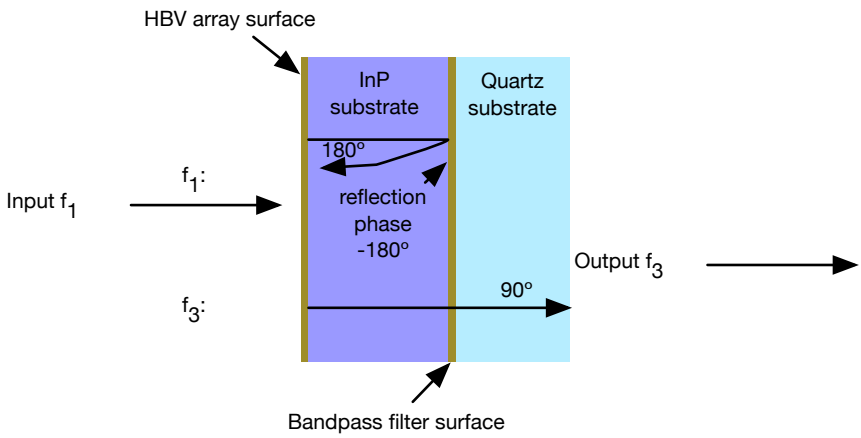

Figure 3.10: Cross-sectional view of the cascaded multiplier elements. From left to right: the 2D HBV grid on a InP substrate followed by the bandpass filter structure on a quartz substrate. The properties are described by two rows explaining the function, one for the input frequency, f_1 and one for the third harmonic frequency f_3.

Since the filter also serves as a heat-sink to the array the thermal properties of the dielectric chosen for the filter need to be considered, especially for the high power application 2D grids we are aiming for. Here quartz was chosen since thermal simulations predict that the InP substrate of the device array in itself would provide sufficient heat

dissipation for the given application, and the impedance of the quartz substrate is close to the geometric mean of the air filled waveguide and the InP varactor substrate at the third harmonic, making it suitable as a $\lambda/4$ output impedance transformer.

3.6 Design of a 184 GHz Schottky diode frequency doubler grid

The Schottky doubler presented in Paper B was designed to fit a 8 by 16 grid of square unit cells in a standard WR-10 waveguide, resulting in 160 μm by 160 μm unit cells, see Figure 3.11. The topology of the frequency doubler is similar to that for the HBV tripler, one set of the cascaded transmission line model used can be found in Paper B. A dielectric slab is used as an input match and simultaneously stops the generated second harmonic from propagating towards the input. The varactor grid is stacked on top of the filter grid, a filter that presents a first order high-pass function. Dipole-like antenna elements are used to couple the input and output wave to the grid and thus a serial bias scheme was the simplest to implement. This meant that the eight varactors in one column were connected to bias distribution lines running along the long side of the array; a fabricated chip is shown in Figure 4.7.

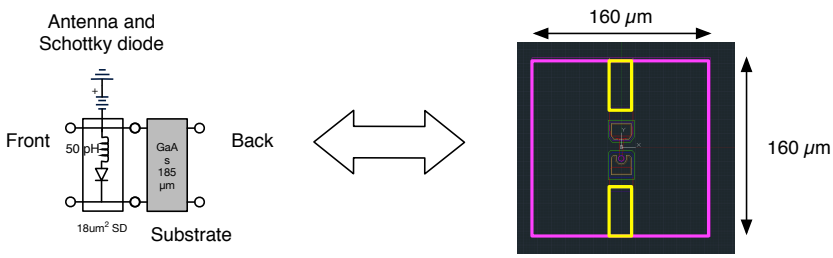

Figure 3.11: Varactor grid cell model together with lump component approximations derived using the induced-EMF method.

The design was aiming to achieve peak conversion efficiency with 1 W of input power at 92 GHz pump frequency. The simulated vector summed conversion efficiency as a function of output frequency is plotted in Figure 3.12. With 1 W of input power the simulated 3 dB bandwidth is 7.5 %. Similarly, a number of conversion efficiencies at 184 GHz output frequency are plotted as a function of input power in Figure 3.13. The naming convention of the columns follows that of the HBV tripler, where column a is the one closest to the central symmetry line, b is one step further out, etc.

To achieve a compact implementation a module based on three 3 mm thick shims was designed. In the first shim the input matching substrate is mounted, the second shim houses the varactor grid, filter and bias network. A stepped output taper was

chosen to transform the output second harmonic from the input WR-10 to the output WR-5.1 waveguide interface. The use of a stepped instead of linear taper greatly reduces the length of the output transformer, thus making it possible to fit it into the third 3 mm thick shim. An exploded view of the shim system and all the internal components is given in Figure 3.14.

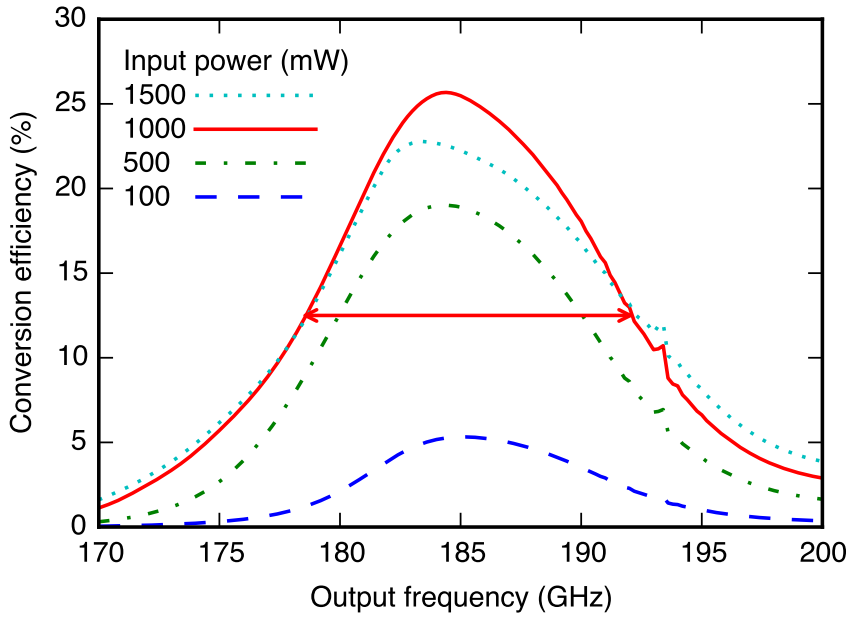

Figure 3.12: Simulated vector summed conversion efficiency for the complete module as a function of output frequency for different input powers.

3.7 Waveguide cavity design

The most common way of realising multipliers and other THz circuits is by what is commonly referred to as E-plane split blocks. A waveguide block machined in this fashion typically consists of two milled halves where the waveguide has been split along the E-field symmetry plane, for the H_{10} mode standard rectangular waveguide with a 2:1 ratio between the walls, which means that the two halves will have a quadratic cut. Since no surface currents flow across this plane on the waveguide wall the method is rather insensitive against poor electrical connection between the waveguide halves. Conventional THz circuits are typically mounted in one of the waveguide block halves

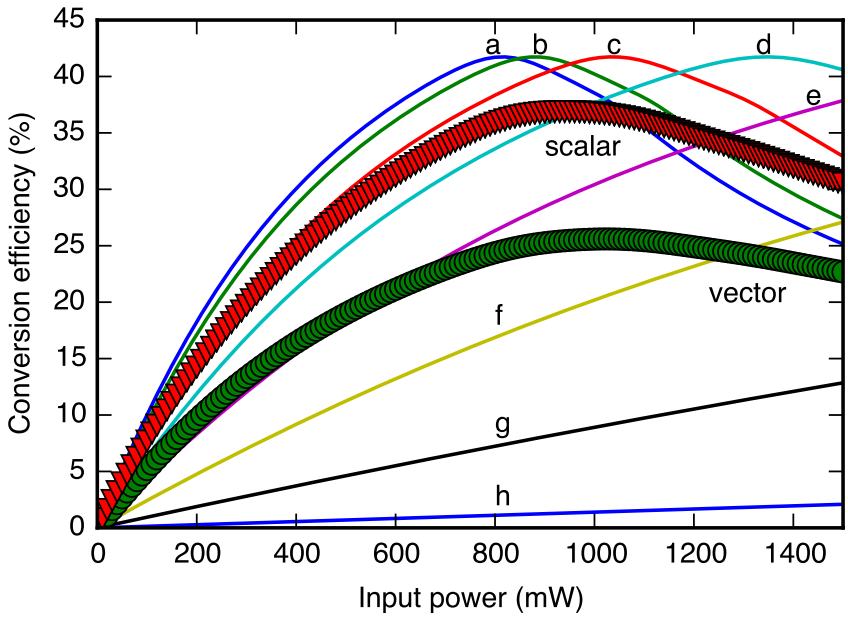

Figure 3.13: Simulated conversion efficiency for the eight columns as a function of input power. The calculated vector summed efficiency and scalar summed efficiency are also plotted. All data are for 184 GHz output frequency.

and couple to the propagating wave in the waveguide by E or H field probes. When mounting such circuits all work can be done in one of the halves and then the other half of the waveguide can be attached.

The fabrication of waveguide packaged components becomes increasingly difficult at frequency approaching the terahertz region. One of the main reasons for this is that the waveguide dimensions shrink to the order of hundreds of micrometers making it hard to machine with sufficient precision and surface finish even when using modern computer controlled mills. Assembling such circuits with high yield requires precision in the micrometer range.

For quasi-optical components designed to couple directly to the propagating wave the E-plane split block manufacturing technique described earlier becomes problematic. If all components are mounted in one half of an E-plane split block extreme care must be taken when mounting the other waveguide half or the arrays will be shattered. Another problem is the poor thermal contact since there is no natural way of thermally attaching the waveguide to the multiplier chip. One approach could be to apply the waveguide

split in an another plane, such as in [49], but at frequencies in the THz range such a waveguide split can cause large ohmic losses and degrades efficiency.

In this work a shim system has been used instead, where the different parts are mounted in interchangeable shims. Since the shims are relatively thin, tooling exists to machine the shims from the direction of the propagating wave, making machining easier. Figure 3.14 shows an exploded view of the shim system used for the Schottky doubler. After the parts are inserted in the shim a thermal glue is applied in the round corner pockets and along the short side of the array, securing the assembled package in the shim and enhancing thermal conduction.

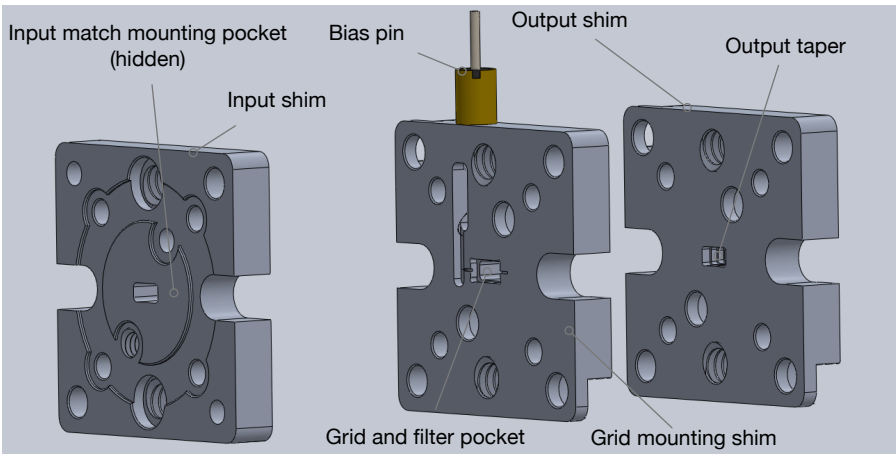

Figure 3.14: Exploded view of the shim system used for the X2 frequency multiplier.

3.8 Filters and matching elements for free space operation of the HBV frequency tripler grid

For free space operation a simpler matching circuit made for plane wave operation is designed. It is based on two available commercial bandpass filters fabricated as a copper foil. One filter has its centre frequency at the 83 GHz input tone and the other at the 249 GHz output harmonic. Since no simulation data was available for the filters the matching strategy is to have a setup where the distance between the filters and the array can be varied, thereby finding the positions where the output filter acts as a back-short for the input harmonic and the input filter reflects the part of the third harmonic that propagates in the wrong direction. The full varactor substrate thickness of $635\mu m$ is used in the matching circuit that can be seen in Figure 3.15

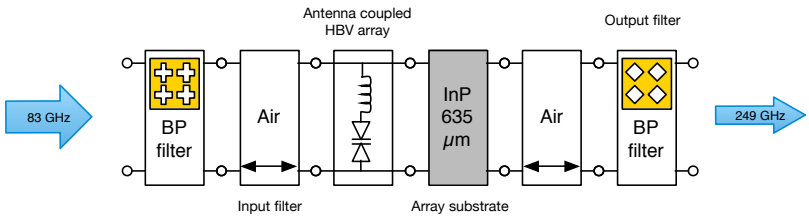

Figure 3.15: A complete unit cell transmission line model of the free space operating frequency tripler 2D array. Two-position adjustable bandpass filters are used to tune the circuit.

Chapter 4

Fabrication and characterisation of varactor grid frequency multipliers

Fabrication and characterisation are both important steps in the development of state of the art circuits. This chapter explains the fabrication steps employed in the production of the varactor grids in Paper A and B. The standard III-V processing is described in detail for the HBV grid and more briefly for the Schottky grid since many of the fabrication steps are similar. Finally the measurement methods used for RF characterisation will be discussed.

4.1 Varactor grid fabrication

This section outlines the fabrication steps used to produce the HBV grids by means of a series of pictures. All the main process steps are covered, for a detailed process plan see Appendix A. The renderings in Figure 4.1 to Figure 4.4 explain the process steps with focus on a cross section of one unit cell at the chip, with the exception of the last where the cross section cut is removed and the unit cell is displayed from above. The fabrication was done on two chips with the dimensions 19 mm by 19 mm. Each chip contained twenty 6 by 12 unit-cell 2D grids suited for WR-10 waveguide mounting and two 33 by 33 arrays for free space tests. The 6 x 12 2D grids were then sawn into 2.54 mm x 1.27 mm dies and lapped to 200 μm thickness resulting in arrays such as the one shown in Figure 4.5. A scanning electron microscope picture of a part of the array is also shown in Figure 4.6.

The fabrication of the Schottky varactors is similar to the HBV varactor fabrication described above, with the exception of the Schottky contact deposition and different

etch steps. A photograph of a finished chip and a SEM picture of a unit cell is shown in Figure 4.7 and Figure 4.8 respectively.

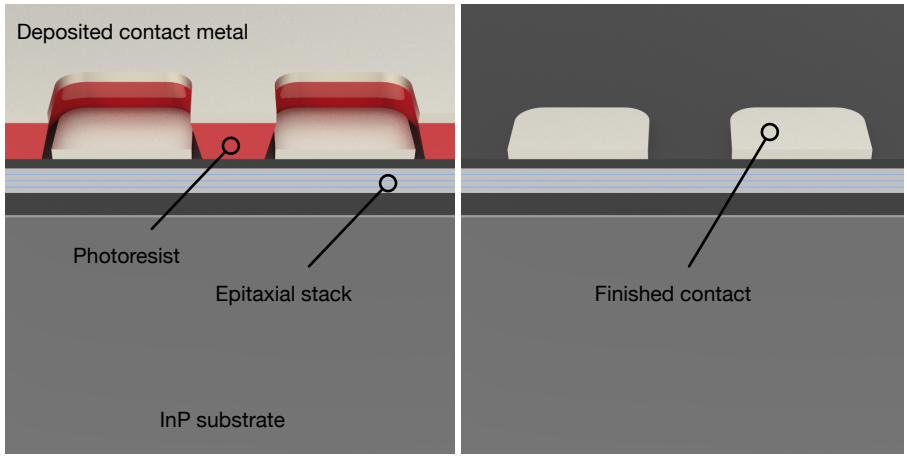

Figure 4.1: Left: Patterning with photoresist followed by contact metal deposition. Note the negative slope of the photoresist that enables lift-off of the excess metal. Right: Finished contacts after lift off and removal of the photoresist.

4.2 Filter fabrication and substrate thinning

Two different fabrication approaches have been used for the filters, e-beam evaporation and electroplating. The steps employed for the circuit fabrication are thus identical to the contact patterning steps in Figure 4.1 and circuit patterning step in Figure 4.3.

Since the substrates of both the varactor grids and the filters are used as transmission lines the final thickness of every part is important. The filters and grids are fabricated on substrates with thicknesses ranging from 380 μm to 630 μm, thus the final components need to be diced into small chips with the correct dimensions and lapped to the correct thickness. Dicing and lapping was done in the same way for both varactor grids and filters. First, dicing trenches were cut on the device side of the sample down to a depth corresponding to the final thickness of the chips. This was done using a CNC dicing saw equipped with a 50 μm wide dicing blade. Then the chips were attached to a lapping chuck using a crystal wax with a melting temperature of 70° C. The chips were then hand lapped to the correct thickness with the help of a flat glass plate and 3 μm calcinated silicon carbide abrasive powder dissolved in water. Warm acetone was then used to dissolve the wax and release the finished chips.

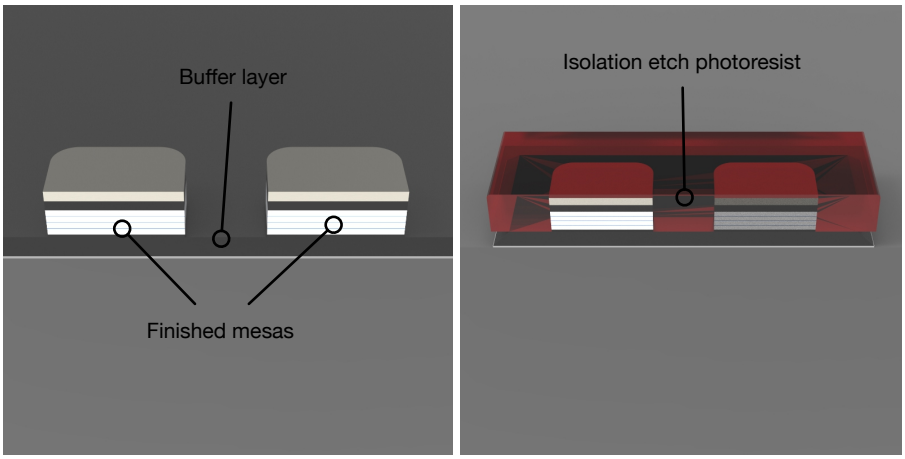

Figure 4.2: Left: Finished mesas after dry etch. The dry etch is anisotropic, thus the top contacts are sufficient to protect the mesa. Right: Patterning with photoresist followed by wet etching to remove excess buffer layer. The parts of the buffer layer that is used to connect the mesas are protected by the photoresist. Note the undercut beneath the resist edge, an effect created by the isotropic wet etch.

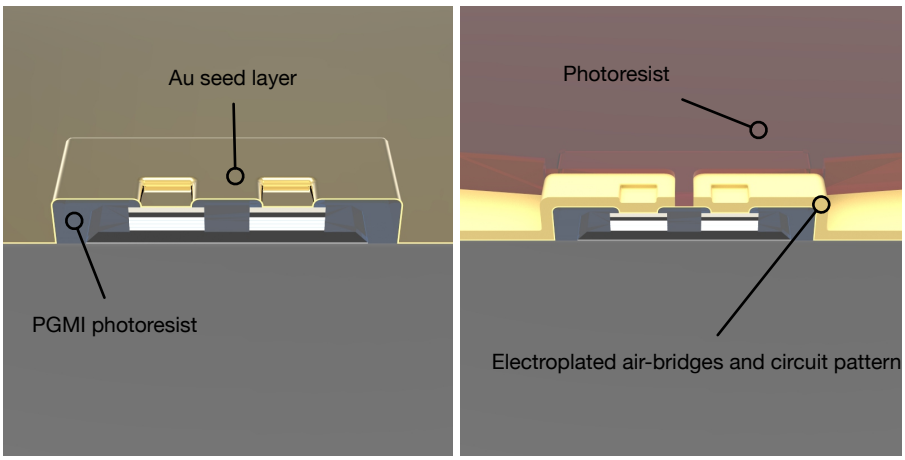

Figure 4.3: Left: Patterning of PGMI photoresist used to support the air-bridges. This is followed by sputtering of a gold seed-layer used to enable electroplating of the bridges and circuit pattern. Right: Patterning with thick photoresist and electroplating of air-bridges and circuit pattern.

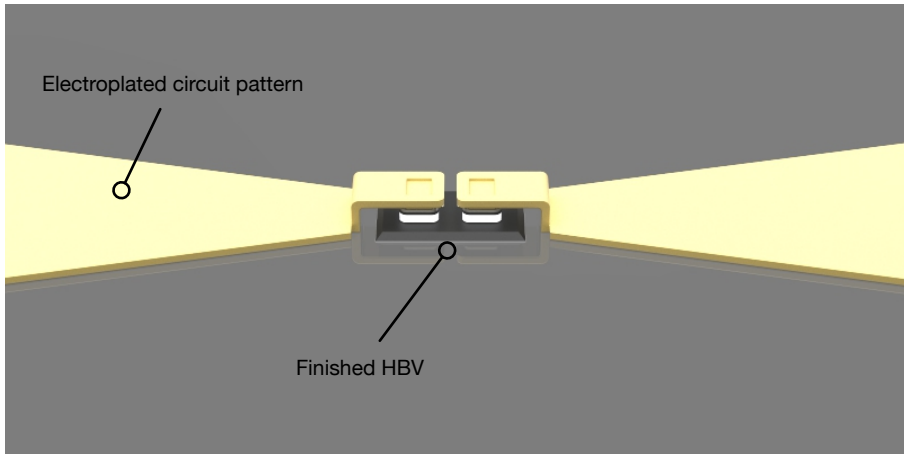

Figure 4.4: Partial view of a finished unit cell after removal of the photo resist and excess seed layer.

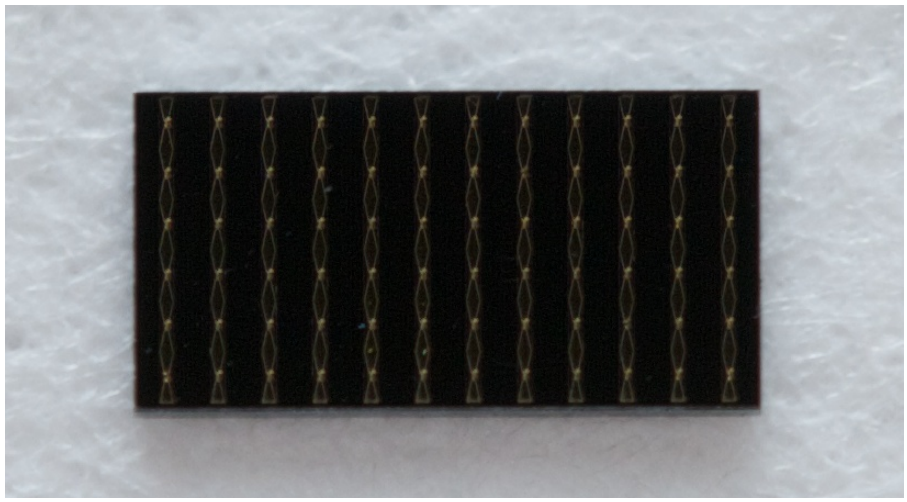

Figure 4.5: Photograph of a manufactured 6 x 12 HBV grid.

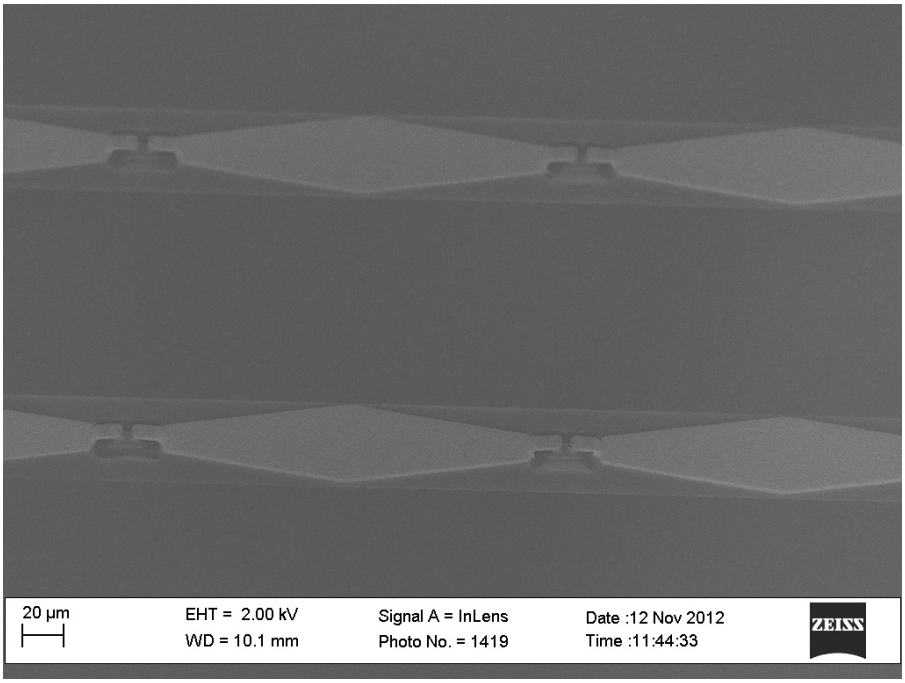

Figure 4.6: Scanning electron microscope picture of a part of one of the HBV grids. Note the four two-mesa air-bridge contacted HBV varactor diodes.

4.3 Waveguide measurement setup

To characterise the grid multipliers two measurement systems were assembled. For the tripler grid in Paper A a measurement setup built around two GaN power amplifier was built, a block diagram is shown in Figure 4.9. The power amplifier is fed through a chain consisting of a microwave synthesiser, a x6 frequency multiplier, two amplifiers where the last one was changed depending on the measured frequency band and an isolator. On the output of the amplifier a circulator is attached to isolate the power amplifier from the sometimes highly reflective multiplier device under test (DUT). The return port of the circulator is simultaneously used to measure the reflected power, while the forward power is measured with a calibrated diode detector through the directional coupler. The output power from the DUT is measured by a calorimetric power sensor through a WR-03 to WR-10 waveguide taper. The first taper is used to create a single mode H_{10} output from the frequency multiplier while the second taper matches the output of the multiplier to the WR-10 input of the power detector. The short section of WR-03 waveguide between the tapers also serves as a 170 GHz high-pass filter, effectively blocking any pump frequency signal from reaching the output

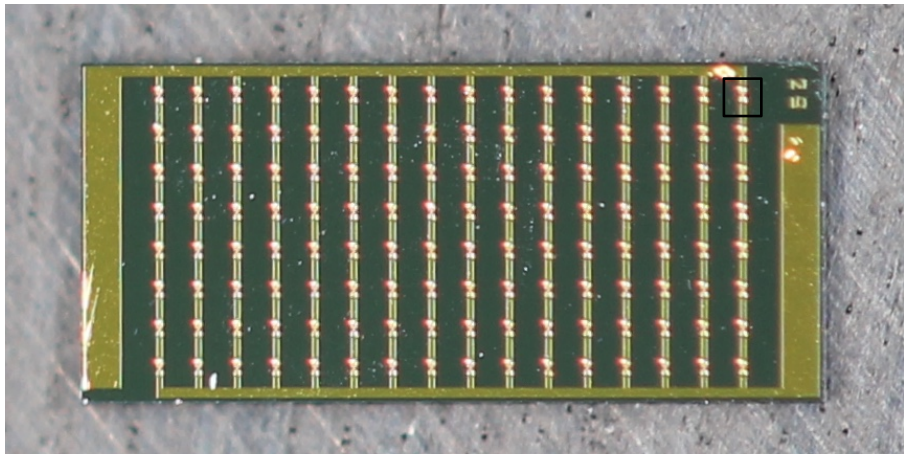

Figure 4.7: Photograph of a fabricated Schottky varactor grid. Note the bias distribution lines running along the top and bottom sides of the substrate. A unit cell is also marked with a black rectangle.

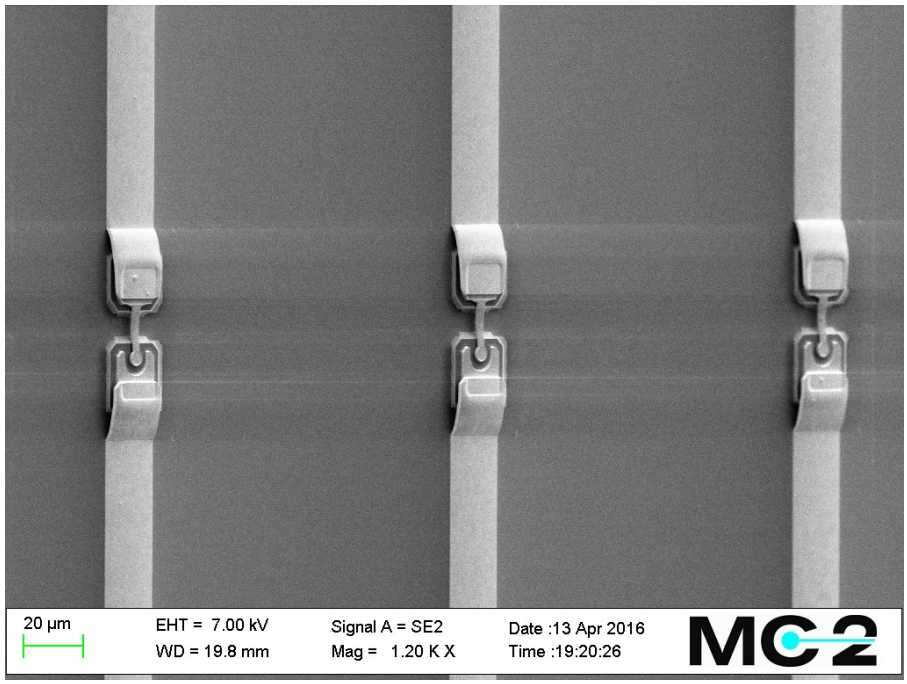

Figure 4.8: A magnified SEM view of three varactor diodes and unit cells.

power detector. A photograph of the setup can be seen in aper A, Figure 7.

Te measurement system used to characterise the doubler in Paper B is presented in Figure 4.10 with a photograph and a block diagram. The main difference between the other system is the use of a different power amplifier.

Since the power amplifiers are driven into saturation, harmonics could potentially be generated and incorrectly interpreted as an output signal from the multiplier. To test this the multiplier grid was replaced by a dummy InP chip while the amplifier was operated under the same conditions as during the actual tests. The harmonic content was not measurable or $<<$ 1% of the measured output power from the multiplier. Another potential source of error are output signals from the multiplier at higher frequencies than the desired harmonic since the detector is sensitive well up into visible light frequencies. For the multipliers measured here the third and second harmonic respectively are the desired output signals but some power may also be generated at higher harmonics, however this has not yet been investigated. Infrared radiation, originating from chip heating during measurements, has been excluded as an error source by comparative measurements with IR-absorbing material in the waveguide.

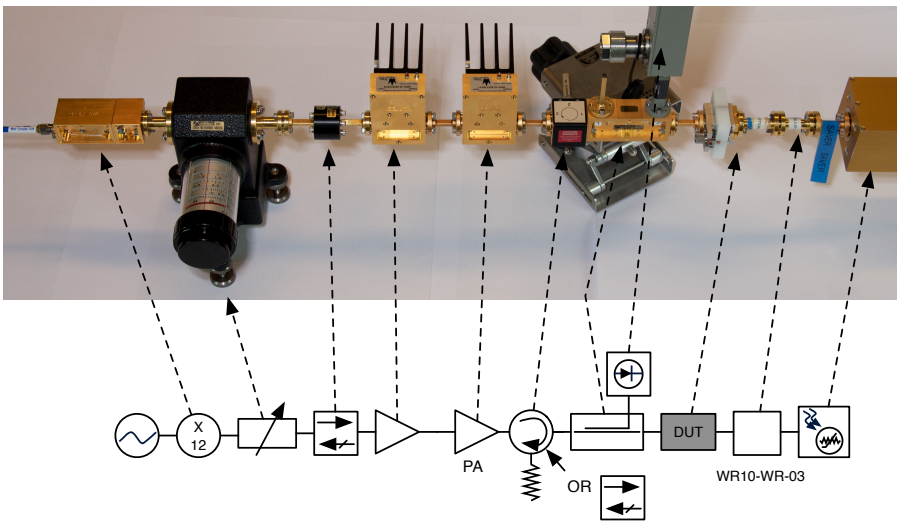

Figure 4.9: A block diagram and photo of the measurement setup used to characterise the tripler grid in Paper A. From Paper A.

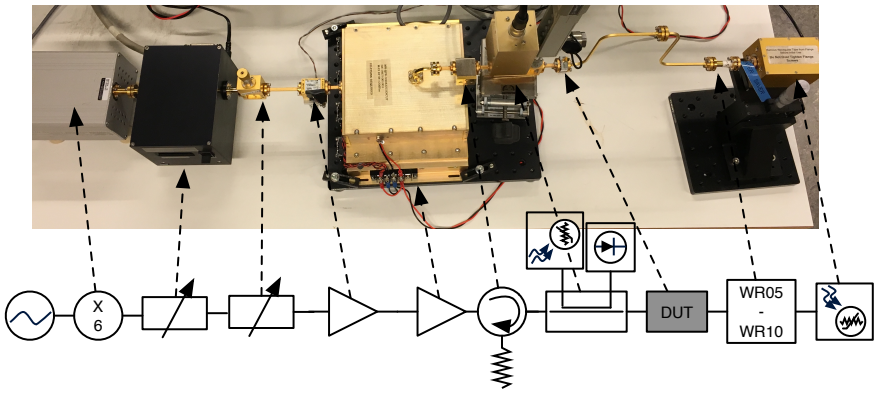

Figure 4.10: Photograph and block diagram of the measurement setup used to characterise the doubler grid in Paper B.

4.4 Free space measurement setup

A measurement setup built to test the larger 33 x 33 array under free space conditions is shown in Figure 4.11. The output from the power amplifier (83 GHz 500 mW) is transmitted through a corrugated horn and then focused by two off-axis parabolic mirrors onto the HBV 2D array. Surrounding the array are the two bandpass filters described in Section 3.8 mounted on linear adjustment stages enabling the distance between the filters and the array to be varied. The output power is sampled by a diode detector mounted on a three axis micrometer stage. By moving the stage the output beam was sampled in the E- and H-plane at various distances from the array. The output from the multiplier 2D array has a Gaussian power distribution, just as expected. By fitting a Gaussian beam to the measured data and then integrating the power in the fitted beam the total output power can be estimated to be 0.6 mW. This yields a very low conversion efficiency, approximately 0.1 %, that is explained by the fact that the input beam power density is Gaussian shaped and covers the 1089 HBV diode 2D array with approximately 90 % spillover efficiency. Thus the power delivered to the individual varactors is low, explaining the low conversion efficiency.

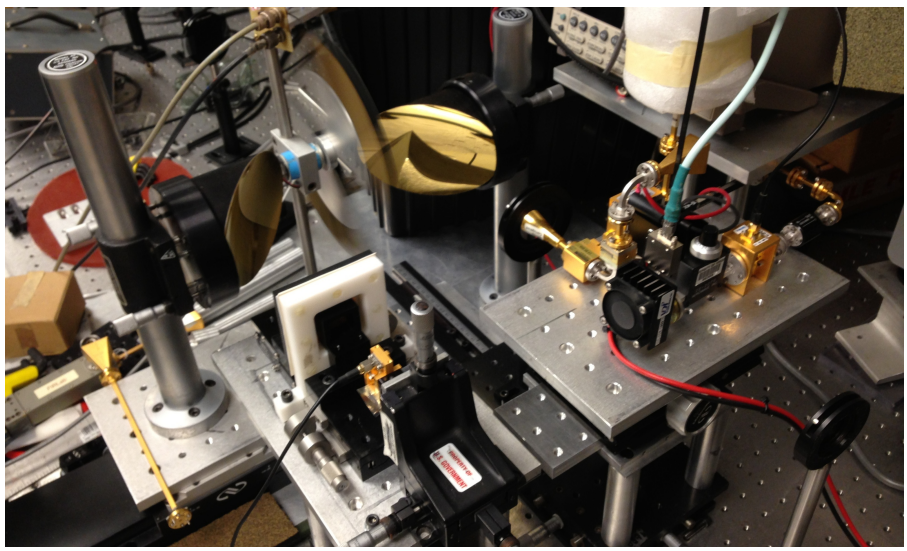

Figure 4.11: Photograph of the free space test setup, the 2D array under test is mounted in the white plastic holder in the left part of the image. The input power radiated from the horn antenna in the upper right part of the picture is focused to the array by two parabolic mirrors. Surrounding the array are the two adjustable filter holders. The diode detector used to sample the output power can be seen on the three axis adjustable stage.

Chapter 5

Imaging applications

In conjunction with the development of grid frequency multipliers, imaging applications that could benefit from high power sources have been researched. Two application examples are included, one aiming at sample investigation at close range and one where a capable FMCW radar chain has been packaged in mechanics enabling imaging array integration.

5.1 A System for THz Imaging of Low-Contrast Samples

In Paper D a THz imaging system built for biological sample investigation is presented. Samples exhibiting high water contents of thicknesses up to 200 μm can be scanned for contrasts in the dielectric properties. An image reconstruction algorithm based on the Born approximation is used to reconstruct the complex permittivity of the sample in the imaging region. The reconstruction algorithm used creates imaging voxels, three dimensional pixels, of 0.1 $mm \times 0.1$ mm (approximately 1/10 of the free space wavelength) in the planar direction, and the whole thickness of the sample is assumed to have the same properties within the voxel.

To illustrate the performance of the imaging system an imaged leaf, from Paper D, together with measured raw amplitude data and reconstructed complex permittivity is shown in Figure 5.1. Biological samples often have a high concentration of water which means that they are very lossy at THz frequencies. This is the main reason for the 200 μm sample thickness limit of the imaging system. The leaf used in this example was rather dry, thus making it possible to image a slightly thicker sample with good results. With more input power, which is the goal of the work in this thesis, thicker samples with higher moisture content could be imaged. Another route towards a more dynamic range is to increase the sensitivity in the receiver chain.

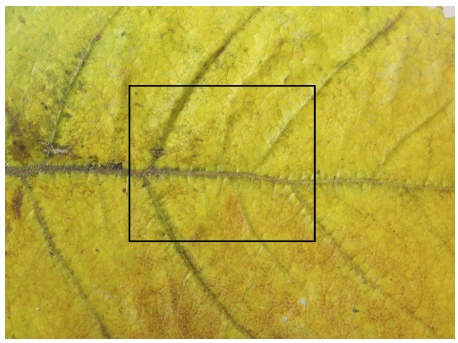

(a) Photograph of the leaf being imaged, the rectangle shows the imaged section.

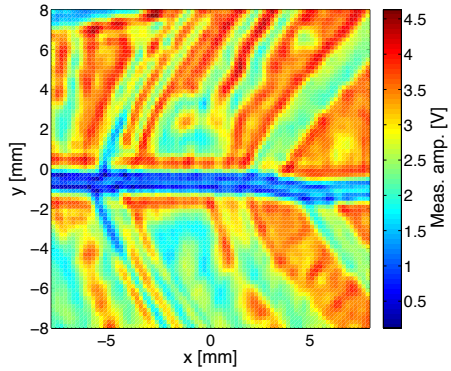

(b) Measured amplitude

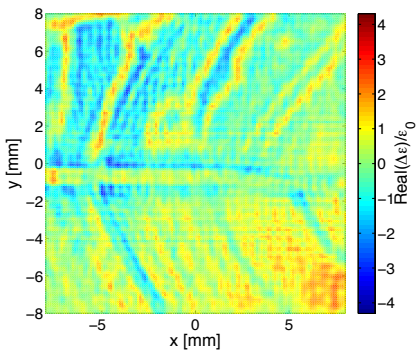

(c) Real part of $\Delta\epsilon$

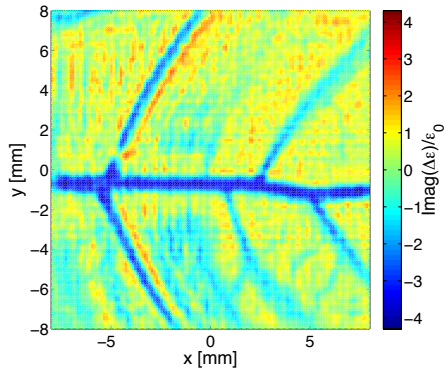

(d) Imaginary part of $\Delta\epsilon$

Figure 5.1: The leaf being imaged is shown in (a). The measured amplitude (unprocessed data) is shown in (b) and the real and imaginary parts of the contrast in relative permittivity are shown in (c) and (d). From Paper D.

By having more power available at THz frequencies, the applicability of THz imaging would be widened, allowing for more diverse geometries and materials to be scanned with increased dynamic range. These power requirements at THz frequencies could be met by the inherent power combining nature of 2D grids of frequency multipliers. Grids, such as the ones featured in this report, could be utilised as a pump source at sub-mm (over 300 GHz) frequencies or as cascaded arrays to produce high power at THz frequencies. Thus imaging setups similar to that presented here could be constructed, with a higher dynamic range and at even higher frequencies could be possible.

The goal is to use the system to scan histopathological cancer samples and determine the tumour boundary. THz radiation is particularly suitable for this due to the higher absorption of the water retentive cancerous tissue. However the acquisition of test samples having an appropriate thickness has so far been problematic.

5.2 Integration of a 340 GHz radar-array transceiver module

In Paper E a novel integration scheme enabling FMCW radar array construction is presented. A state of the art RF chain is integrated in modularised mechanics enabling the construction of one or two dimensional arrays. Sixteen modules will be produced for the European "Concealed Object Stand-Off Real-Time Imaging for Security" project, intended to serve as a technology demonstrator for stand-off radar imaging for security applications. Each module represents a pixel-channel in the imaging system and a mechanical scanner is used to sweep the focused pixels over the target, thereby creating an image. Since the imaging radar uses a mechanical system to scan over the target each extra transceiver chain will reduce the number of positions needed in the mechanical scanner to create an image, thus decreasing the image capture time. The relatively high output over the transmit band and good receiver sensitivity enables short integration times for each measurement and thereby allows fast mechanical scanning of the focused beam.

In Figure 5.2 the top halves of the blocks have been removed to show the internal features not visible in Paper E. In the first module the X8 MMIC is mounted together with a waveguide probe and an experimental bias PCB used to fine tune the performance of the X8 chip. The second module houses the 170 GHz Schottky doubler and its supporting bias circuits. The third module contains all parts of the transceiver circuit, input and output hybrid couplers, two Schottky transceiver chips, supporting IF electronics and the output waveguide flange. In the bottom PCB lid of all three modules the bias distribution network is routed.

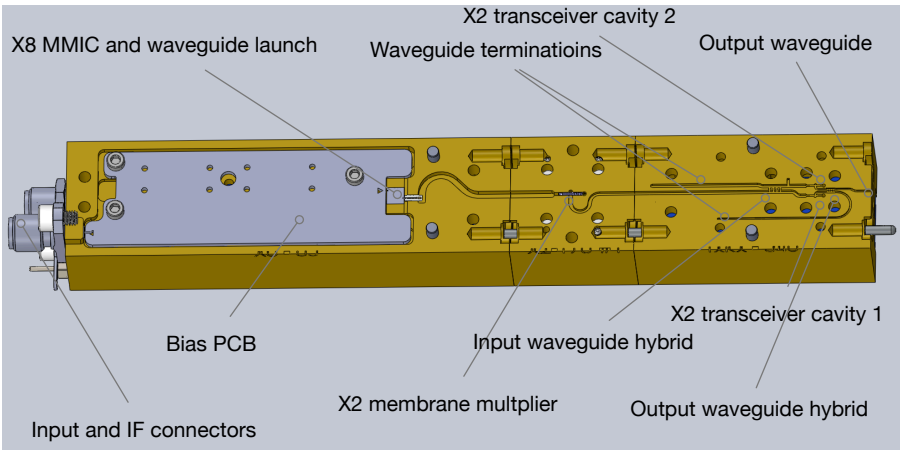

Figure 5.2: The transceiver chain waveguide blocks with the upper halves removed.

Chapter 6

Conclusions and future outlook

The two presented grid frequency multiplier modules deliver state-of-the-art performance in terms of operating frequency, output power and conversion efficiency for comparable technology. Paralleled sets of cascaded unit cells have proven to be a computationally efficient and reliable design method. However, to fully analyse a particular design, a full 3D model together with a complete analysis of all nonlinear elements is needed. Alternatively, it is possible that additional complements to the unit cell modelling approach could achieve the same result. Even though the full 3D simulation offers the best prediction of the multiplier modules performance so far, limitations still exist, e.g. the accuracy of the nonlinear models and the ability to model losses in metals and dielectrics properly. Slight tilts of the mounted components or uneven thicknesses of the substrates caused by the processing are hard to incorporate in the simulation.

A problem noted during the measurements is the spurious response as a function of frequency, this is most evident in Paper B. What seems to be the same phenomena can also be observed in previously published work [50]. Thera are many possible explanations to the frequency response seen, among them:

- The excitation of substrate modes due to the dimensions of the substrate or the circuit pattern on it.
- The waveguide cavity has sharp steps and pockets that could launch unwanted modes or even cause a leak of RF energy.
- Trapped modes within the structure [97].
- Even though great care has been taken to thin the substrates to an even thickness all substrates seems to have a slope of a few microns. This could be enough to launch substrate modes.
- It is hard to mount with a precision of a few microns, misalignments or tilts in the mounting could cause a resonant behaviour.

- A varactor column is only a few unit cells high, there is a possibility for resonances along the column.

Increasing the conversion efficiency of grid frequency multipliers is an other important research topic, some of the commonly proposed solutions are summarised below:

- Even out the conversion efficiency by tapering the size of the diodes, i.e. use different diode sizes in different positions of the grid.
- Taper the size of the unit cells to create a grid with non-uniform unit cells.
- Even out the input power by using a corrugated waveguide structure that supports a TEM wave.
- Excite the waveguide structure with a composition of modes, like in [98].

Energy launched into other modes than the H10 is hard to transform to a single H10 mode output. The diode size affects the diode impedance and thus the output phase of the generated harmonic. An even conversion efficiency among different sized diodes may therefor not couple to the output mode in phase. Different sized unit cells may cause the same problem.

During fabrication of waveguide embedded frequency multipliers it is essential that the thickness of the substrates used as transmission lines can be controlled down to the micrometer scale. Similarly important is that the components can be mounted with high precision and without unintentional tilt that may otherwise launch unwanted modes or cause other problems. A potential solution to the sensitivity in thickness and mounting tolerances could be to use epitaxial transfer to silicon in order to get access to the micro machining toolbox. Waveguides and matching structures could then be lithographically defined with very high precision.

There are many ways forward in the field of 2D frequency multiplier arrays, one of the most important being straight forward design methods. If a unified, accurate, design method could be outlined the technology has a great potential to provide the high power THz sources of the future.

Imaging applications are advancing rapidly, to a large extent driven by the increasing availability of THz sources and detectors. As sources and receivers become more compact and affordable the number of applications will likely rise. Quasi-optical mixer arrays have been demonstrated previously [99]. A future development of the 2D-grid frequency multipliers could be to implement a similar transceiver structure as presented in Paper E and originally presented in [100]. This could enable a new generation of high power THz radar transceivers.

Acknowledgement

First of all I would like to express my gratitude to my examiner Prof. Jan Stake and supervisor Dr. Josip Vukusic who have given me support and the opportunity to work in this exciting field. My co-supervisors Dr. Tomas Bryllert and Dr. Peter Sobis have guided me through many technical difficulties for which I am grateful.

But this journey would probably not have started if it was not for my grandfather Mats Johansson who introduced me to transistor circuits at an early age. Both Tonny Rubæk and Gergely Hrubo have contributed greatly with their knowledge and effort during our joint projects. I would also like to thank Johanna Hanning, Arvid Hammar and all colleagues at the Terahertz and Millimetre Wave Laboratory for giving me such a fun and inspiring work environment. Without Carl-Magnus Kihlman and Mats Myremark with their machining experience many of my crazy ideas had not been possible to realise. Catharina Forssen and the administrative staff at the Department of Microtechnology and Nanoscience deserves a special thank for making all my projects run smoothly. Peter Langsdale deserves a special thank for his help with proofreading the thesis.

I would also like to thank Dr. Tapani Närhi at ESA for helpful discussions on the topic of frequency multiplier 2D grids.

I am grateful to Prof. Robert M. Weikle II who gave me the opportunity and guidance to deepen my knowledge in unit-cell modelling and quasi-optical measurements during my five months at the University of Virginia. A special thank goes to Alexander Arsenovic, Matt Bauwens, Michael Cyberey and all my colleagues at UVa for making my stay unforgettable.

Last but not least I would like to thank my wife Edna for all her love and support during this work and Lycke for motivating me to finish. I am also grateful to my family for all their care and visits during my years at Chalmers.

This research was financially supported by the Swedish Research Council, VR, the European Space Agency, ESA and The Swedish Foundation for Strategic Research, SSF.

Robin Dahlbäck

Göteborg
May 2016

Chapter 7

Author contribution to appended papers

Paper A

"A tunable 240 — 290 GHz waveguide enclosed 2D-grid HBV frequency tripler," *IEEE Transactions on Terahertz Science and Technology*, vol. 6, no. 3, May 2016.

Contributions: I designed the module and the circuits. This includes 3-D electromagnetics/thermal and electrical circuit design, cleanroom fabrication, assembly and DC/RF characterisation. I also wrote the paper.

Paper B

"A compact 128 Schottky diode grid frequency doubler generating 0.25 W of output power at 183 GHz.," submitted to *IEEE Microwave and Wireless Components Letters*, April 2016.

Contributions: I did the design, the assembly and characterisation and part of the fabrication. I also wrote the paper.

Paper C

"Full 3D Modeling of Waveguide Embedded Frequency Multiplier Arrays.," submitted to *IEEE Microwave and Wireless Components Letters*, March 2016.

Contributions: I developed the unit cell modelling and design of the multiplier. Collaborated on the development of the full 3D model. Designed the mechanics and fabricated semiconductor components in the cleanroom. Assembled and measured the multipliers together with co-authors. Co-wrote the paper.

Paper D

"A System for THz Imaging of Low-Contrast Targets Using the Born Approximation,"*IEEE Transactions on Terahertz Science and Technology*, vol. 2, no. 3, pp. 361-370, April 2012.

Contributions: I developed and assembled the imaging system with custom built RF and hardware components. Performed measurements and co-wrote the paper.

Paper E

"Compact 340 GHz homodyne transceiver modules for FMWC imaging radar arrays," *International Microwave Symposium*, May 2016, San Francisco, CA, USA.

Contributions: I designed the submodules including mechanical outline, implemented waveguide circuits, interconnects, bias circuits. Performed measurements and wrote the paper.

References

[1] D. L. Sengupta, T. K. Sarkar, and D. Sen, "Centennial of the semiconductor diode detector," *Proceedings of the IEEE*, vol. 86, pp. 235–243, Jan. 1998.

[2] E. Pickwell and V. P. Wallace, "Biomedical applications of terahertz technology," *Journal of Physics D: Applied Physics*, vol. 39, pp. R301–R310, Aug. 2006.

[3] P. F. Taday, "Applications of terahertz spectroscopy to pharmaceutical sciences," *Philosophical Transactions of the Royal Society A: Mathematical, Physical and Engineering Sciences*, vol. 362, pp. 351–364, Feb. 2004.

[4] F. C. De Lucia, "The submillimeter: A spectroscopist's view," *Journal of Molecular Spectroscopy*, 2010.

[5] H. J. Hansen, "Standoff Detection Using Millimeter and Submillimeter Wave Spectroscopy," in *Proceedings of the IEEE*, pp. 1691–1704, 2007.

[6] N. Gopalsami and A. C. Raptis, "Remote detection of chemicals by millimeter-wave spectroscopy," *SPIE's International Symposium on Optical Science, Engineering, and Instrumentation*, vol. 3465, pp. 254–265, Nov. 1998.

[7] N. Shimizu, H. J. Song, Y. Kado, T. Furuta, and A. Wakatsuki, *Gas detection using terahertz waves.* NTT Technical Review, 2009.

[8] M. Tonouchi, "Cutting-edge terahertz technology," *Nature Photonics*, vol. 1, pp. 97–105, Feb. 2007.

[9] N. Gopalsami, S. Bakhtiari, T. W. Elmer II, and A. C. Raptis, "Application of Millimeter-Wave Radiometry for Remote Chemical Detection," *IEEE Trans. Microw. Theory Techn.*, vol. 56, no. 3, pp. 700–709, 2008.

[10] W. Shi and Y. J. Ding, "Identification of chemicals in the vapor phase by directly measuring absorption spectra through frequency-tuning a monochromatic THz source," in *Optics East* (J. O. Jensen and J.-M. Theriault, eds.), pp. 11–15, SPIE, Dec. 2004.

[11] P. Buaphad, P. Thamboon, C. Tengsirivattana, J. Saisut, K. Kusoljariyakul, M. W. Rhodes, and C. Thongbai, "Progress on Reflective Terahertz Imaging for Identification of Water in Flow Channels of PEM Fuel Cells," *Applied Mechanics and Materials*, vol. 110-116, pp. 2301–2307, Oct. 2011.

[12] W. L. Chan, J. Deibel, and D. M. Mittleman, "Imaging with terahertz radiation," *Reports on Progress in Physics*, vol. 70, pp. 1325–1379, July 2007.

[13] S. Kharkovsky, J. T. Case, M. A. Abou-Khousa, R. Zoughi, and F. L. Hepburn, "Millimeter-Wave Detection of Localized Anomalies in the Space Shuttle External Fuel Tank Insulating Foam," *IEEE Transactions on Instrumentation and Measurement*, vol. 55, pp. 1250–1257, Aug. 2006.

[14] T. Bryllert, K. B. Cooper, R. J. Dengler, N. Llombart, G. Chattopadhyay, E. Schlecht, J. Gill, C. Lee, A. Skalare, I. Mehdi, and P. H. Siegel, "A 600 GHz imaging radar for concealed objects detection," in *2009 IEEE Radar Conference*, pp. 1–3, IEEE, 2008.

[15] K. B. Cooper and G. Chattopadhyay, "Submillimeter-Wave Radar: Solid-State System Design and Applications," *IEEE microwave magazine*, vol. 15, no. 7, pp. 51–67, 2014.

[16] K. Cooper, R. Dengler, N. Llombart, T. Bryllert, G. Chattopadhyay, E. Schlecht, J. Gill, C. Lee, A. Skalare, and I. Mehdi, "Penetrating 3-D Imaging at 4-and 25-m Range Using a Submillimeter-Wave Radar," *IEEE Trans. Microw. Theory Techn.*, vol. 56, no. 12, Part 1, pp. 2771–2778, 2008.

[17] C. Am Weg, W. von Spiegel, R. Henneberger, R. Zimmermann, T. Loeffler, and H. G. Roskos, "Fast Active THz Cameras with Ranging Capabilities," *Journal of Infrared, Millimeter and Terahertz Waves*, vol. 30, pp. 1281–1296, Aug. 2009.

[18] G. Chattopadhyay, "Technology, Capabilities, and Performance of Low Power Terahertz Sources," *IEEE Trans. THz Sci. Technol.*, vol. 1, no. 1, pp. 33–53, 2011.

[19] M. S. Vitiello and A. Tredicucci, "Tunable Emission in THz Quantum Cascade Lasers," *IEEE Trans. THz Sci. Technol.*, vol. 1, no. 1, pp. 76–84, 2011.

[20] F. Braun, "Ueber die Stromleitung durch Schwefelmetalle," *Annalen der Physik*, vol. 229, pp. 556–563, Jan. 1875.

[21] A. H. Wilson, "The Theory of Electronic Semi-Conductors," *Proceedings of the Royal Society of London A: Mathematical, Physical and Engineering Sciences*, vol. 133, pp. 458–491, Oct. 1931.

[22] W. Schottky, "Halbleitertheorie der Sperrschicht," *Naturwissenschaften*, vol. 26, no. 52, pp. 843–843, 1938.

[23] H. A. Bethe, "Theory of the boundary layer of crystal rectifiers," tech. rep., Radiation Laboratory, MIT, 1942.

[24] S. William, "Circuit element utilizing semiconductive material," 1951.

[25] A. I. Gubanov, *Theory of the contact of two semiconductors of the same type of conductivity.* Zh. Tekh. Fiz, 1951.

[26] E. Kollberg and A. Rydberg, "Quantum-barrier-varactor diodes for high-efficiency millimetre-wave multipliers," *Electronics Letters*, vol. 25, no. 25, pp. 1696–1698, 1989.

[27] J. H. Booske, R. J. Dobbs, C. D. Joye, C. L. Kory, G. R. Neil, G.-S. Park, J. Park, and R. J. Temkin, "Vacuum Electronic High Power Terahertz Sources," *IEEE Trans. THz Sci. Technol.*, vol. 1, no. 1, pp. 54–75, 2011.

[28] J. Federici and L. Moeller, "Review of terahertz and subterahertz wireless communications," *Journal of Applied Physics*, vol. 107, no. 11, pp. 111101–111101–22, 2010.

[29] T. Idehara, T. Saito, I. Ogawa, and Y. Tatematsu, "High power THz technologies opened by high power radiation sources - gyrotrons," *2010 International Kharkov Symposium on Physics and Engineering of Microwaves, Millimeter and Submillimeter Waves (MSMW)*, 2010.

[30] A. Brown, K. Brown, J. Chen, K. Hwang, N. Kolias, and R. Scott, "W-band GaN power amplifier MMICs," *Microwave Symposium Digest (MTT), 2011 IEEE MTT-S International*, pp. 1–4, 2011.

[31] M. Micovic, A. Kurdoghlian, A. Margomenos, D. F. Brown, K. Shinohara, S. Burnham, I. Milosavljevic, R. Bowen, A. J. Williams, P. Hashimoto, R. Grabar, C. Butler, A. Schmitz, P. Willadsen, and D. Chow, "92-96 GHz GaN power amplifiers," in *2012 IEEE/MTT-S International Microwave Symposium - MTT 2012*, pp. 1–3, IEEE, 2012.

[32] J. Schellenberg, E. Watkins, M. Micovic, B. Kim, and K. Han, "W-band, 5W solid-state power amplifier/combiner," *2010 IEEE MTT-S International Microwave Symposium Digest (MTT)*, pp. 240–243, 2010.

[33] L. A. Samoska, "An Overview of Solid-State Integrated Circuit Amplifiers in the Submillimeter-Wave and THz Regime," *IEEE Trans. THz Sci. Technol.*, vol. 1, no. 1, pp. 9–24, 2011.

[34] D. Pardo, J. Grajal, C. G. Perez-Moreno, and S. Perez, "An Assessment of Available Models for the Design of Schottky-Based Multipliers Up to THz Frequencies," *IEEE Trans. THz Sci. Technol.*, vol. 4, no. 2, pp. 277–287, 2014.

[35] P. Kirby, Y. Li, Q. Xiao, J. L. Hesler, and J. Papapolymerou, "Power combining multiplier using HBV diodes at 260 GHz," in *Microwave Conference, 2008. APMC 2008. Asia-Pacific*, pp. 1–4, IEEE, 2008.

[36] J. V. Siles, B. Thomas, and G. Chattopadhyay, "Design of a high-power 1.6 THz Schottky tripler using 'on-chip'power-combining and Silicon micromachining," *Proceedings of 22 nd International Symposium on Space Terahertz Technology, Tucson.*, 2011.

[37] J. V. Siles and Maestrini, "A Single-Waveguide In-Phase Power-Combined Frequency Doubler at 190 GHz," *IEEE Microw. Wireless Compon. Lett.*, vol. 21, no. 6, pp. 332–334, 2011.

[38] A. Maestrini, J. Ward, J. Gill, C. Lee, B. Thomas, R. Lin, G. Chattopadhyay, and I. Mehdi, "A Frequency-Multiplied Source With More Than 1 mW of Power Across the 840-900-GHz Band," *Microwave Theory and Techniques, IEEE Transactions on*, vol. 58, no. 7, pp. 1925–1932, 2010.

[39] M. P. DeLisio and R. York, "Quasi-optical and spatial power combining," *Microwave Theory and Techniques, IEEE Transactions on*, vol. 50, pp. 929–936, Mar. 2002.

[40] W. Lam, H. Chen, D. Rutledge, C. Jou, and N. Luchmann, "Diode-grids for millimeter-wave phase-shifters and frequency doublers," *Antennas and Propagation Society International Symposium, 1987*, vol. 25, pp. 1190–1193, 1987.

[41] R. M. Weikle II, D. S. Kurtz, and R. F. Bradley, "A Ku-band diode-array frequency tripler," in *IEEE Antennas and Propagation Society International Symposium 1997. Digest (Cat. No.97CH36122)*, (New York, NY, USA), pp. 2456–9, Sch. of Eng. Appl. Sci., Virginia Univ., Charlottesville, VA, USA, IEEE, 1997.

[42] D. Steup, A. Simon, M. Shaalan, A. Grüb, and C. I. Lin, "A quasioptical doubler-array," *International Journal of Infrared and Millimeter Waves*, vol. 17, no. 5, pp. 843–856, 1996.

[43] R. J. Hwu, L. P. Sadwick, N. C. J. Luhmann, D. B. Rutledge, M. Sokolich, and B. Hancock, "Quasi-optical watt-level millimeter-wave monolithic solid-state diode-grid frequency multipliers," *IEEE MTT-S International Microwave Symposium Digest*, pp. 1069–1072 vol.3, 1989.

[44] A. Moussessian, M. Wanke, Y. Li, J.-C. Chiao, J. Allen, T. Crowe, and D. Rutledge, "A terahertz grid frequency doubler," *Microwave Theory and Techniques, IEEE Transactions on*, vol. 46, no. 11, pp. 1976–1981, 1998.

[45] R. J. Hwu, C. F. Jou, N. C. Luhmann, M. Kim, W. W. Lam, Z. B. Popovic, and D. B. Rutledge, "Array concepts for solid-state and vacuum microelectronics

millimeter-wave generation," *IEEE Transactions on Electron Devices*, vol. 36, no. 11, pp. 2645–2650, 1989.

[46] N. Paravastu and R. M. Weikle II, "A 40-80 GHz quasi-optical balanced doubler using nested ring-slot antennas," *Antennas and Propagation Society International Symposium, 2002. IEEE*, pp. 1–4, Feb. 2004.

[47] J. Stake, S. Hollung, L. Dillner, and E. Kollberg, "A 141-GHz integrated quasi-optical slot antenna tripler," *Antennas and Propagation Society International Symposium, 1999. IEEE*, vol. 4, pp. 2394–2397 vol.4, 1999.

[48] S. Hollung, J. Stake, L. Dillner, M. Ingvarson, and E. Kollberg, "A distributed heterostructure barrier varactor frequency tripler," *IEEE Microw. Guid. Wave Lett. (USA)*, vol. 10, pp. 24–26, Jan. 2000.

[49] J. B. Hacker, A. L. Sailer, B. Brar, G. Nagy, R. L. J. Pierson, and J. A. Higgins, "A high-power W-band quasi-optical frequency tripler," *IEEE MTT-S International Microwave Symposium - IMS 2003*, vol. 3, pp. 1859–1862, 2003.

[50] S. A. Rosenau, *Quasi-optical overmoded waveguide frequency multiplier grid arrays.* PhD thesis, University of California Davis, 2001.

[51] D. B. Rutledge, N. S. Cheng, R. York, R. M. Weikle II, and M. P. De Lisio, "Failures in power-combining arrays," *Microwave Theory and Techniques, IEEE Transactions on*, vol. 47, pp. 1077–1082, July 1999.

[52] P. Penfield and R. P. Rafuse, *Varactor Applications.* MIT Press, 1962.

[53] B. Diamond, "Idler Circuits in Varactor Frequency Multipliers," *IEEE Transactions on Circuit Theory*, vol. 10, pp. 35–44, Mar. 1963.

[54] J. M. Manley and H. E. Rowe, "Some General Properties of Nonlinear Elements-Part I. General Energy Relations," in *Proceedings of the IRE*, pp. 904–913, 1956.

[55] R. M. Fano, "Theoretical limitations on the broadband matching of arbitrary impedances," *Journal of the Franklin Institute*, vol. 249, no. 1, pp. 57–83, 1950.

[56] C. H. PAGE, "Frequency Conversion with Positive Nonlinear Resistors," *Journal of Research of the National Bureau of Standards*, vol. 56, no. 4, pp. 179–182, 1956.

[57] A. Uhlir, "The Potential of Semiconductor Diodes in High-Frequency Communications," in *Proceedings of the IRE*, pp. 1099–1115, 1958.

[58] C. B. Burckhardt, "Analysis of Varactor Frequency Multipliers for Arbitrary Capacitance Variation and Drive Level," *Bell System Technical Journal*, vol. 44, no. 4, pp. 675–692, 1965.

[59] R. M. Weikle II, T. W. Crowe, and E. L. Kollberg, "Multiplier and harmonic generator technologies for terahertz applications," *International Journal of High Speed Electronics and Systems*, vol. 13, no. 02, pp. 429–456, 2003.

[60] V. K. REDDY and D. P. NEIKIRK, "High Breakdown Voltage AlAs/InGaAs Quantum Barrier Varactor Diodes," *Electronics Letters*, vol. 29, no. 5, pp. 464–466, 1993.

[61] S. M. Sze and K. K. Ng, *Physics of Semiconductor Devices.* Wiley-Interscience, third ed., 2007.

[62] J. Stake, S. H. Jones, L. Dillner, S. Hollung, and E. L. Kollberg, "Heterostructure-barrier-varactor design," *Microwave Theory and Techniques, IEEE Transactions on*, vol. 48, no. 4, pp. 677–682, 2000.

[63] L. Dillner, J. Stake, and E. L. Kollberg, "Analysis of symmetric varactor frequency multipliers," *Microwave And Optical Technology Letters*, vol. 15, pp. 26–29, May 1997.

[64] K. Krishnamurthi and R. G. Harrison, "Analysis of symmetric-varactor-frequency triplers," *Microwave Symposium Digest, 1993., IEEE MTT-S International*, pp. 649–652, 1993.

[65] L. Dillner, W. Strupinski, S. Hollung, C. Mann, J. Stake, M. Beardsley, and E. Kollberg, "Frequency multiplier measurements on heterostructure barrier varactors on a copper substrate," *Electron Device Letters, IEEE*, vol. 21, pp. 206–208, May 2000.

[66] T. A. Emadi, J. Stake, T. Bryllert, M. Sadeghi, and J. Vukusic, "Optimum barrier thickness study for the InGaAs/InAlAs/AlAs heterostructure barrier varactor diodes," *Applied Physics Letters*, vol. 90, no. 1, p. 012108, 2007.

[67] S. Maas, *Nonlinear Microwave and RF Circuits.* Artec House, Inc., second ed., 2003.

[68] F. A. Padovani and R. Stratton, "Field and thermionic-field emission in Schottky barriers," *Solid-State Electronics*, vol. 9, no. 7, pp. 695–707, 1966.

[69] E. L. Kollberg, T. J. Tolmunen, M. A. Frerking, and J. R. East, "Current Saturation in Submillimeter Wave Varactors," *IEEE Trans. Microw. Theory Techn.*, vol. 40, pp. 831–838, May 1992.

[70] J. Stake, L. Dillner, S. H. Jones, C. Mann, J. Thornton, J. R. Jones, W. L. Bishop, and E. Kollberg, "Effects of self-heating on planar heterostructure barrier varactor diodes," *IEEE Trans. Electron Devices (USA)*, vol. 45, pp. 2298–2303, Nov. 1998.

[71] J. W. Archer, "A Novel Quasi-Optical Frequency Multiplier Design for Millimeter and Submillimeter Wavelengths," *Microwave Theory and Techniques, IEEE Transactions on*, vol. 32, no. 4, pp. 421–427, 1984.

[72] J. W. MINK, "Quasi-Optical Power Combining of Solid-State Millimeter-Wave Sources," *IEEE Trans. Microw. Theory Techn.*, vol. 34, pp. 273–279, Feb. 1986.

[73] D. S. Kurtz, R. M. Weikle II, and R. F. Bradley, "A Ku-band diode-array frequency tripler," *Antennas and Propagation Society International Symposium, 1997. IEEE., 1997 Digest*, 1997.

[74] X. Qin, C. Domier, N. C. Luhmann, H. X. L. Liu, E. Chung, L. Sjogren, and W. Wu, "Millimeter-wave monolithic barrier n-n+ diode grid frequency doubler," *Applied Physics Letters*, vol. 62, no. 14, p. 1650, 1993.

[75] C. F. Jou, W. W. Lam, H. Z. Chen, K. S. Stolt, N. C. Luhmann, and D. B. Rutledge, "Millimeter-Wave Diode-Grid Frequency Doubler," *IEEE Trans. Microw. Theory Techn.*, vol. 36, pp. 1507–1514, Nov. 1988.

[76] H. X. L. Liu, L. B. Sjogren, C. W. Domier, N. C. Luhmann, D. L. Sivco, and A. Y. Cho, "Monolithic quasi-optical frequency tripler array with 5-W output power at 99 GHz," *Electron Device Letters, IEEE*, vol. 14, pp. 329–331, July 1993.

[77] D. Steup, A. Simon, M. Shaalan, A. Grüb, and C. I. Lin, "A quasioptical, doubler-array," *International Journal of Infrared and Millimeter Waves*, vol. 17, pp. 843–856, May 1996.

[78] P. Siegel, "Terahertz technology in biology and medicine," *IEEE Trans. Microw. Theory Techn.*, vol. 52, no. 10, pp. 2438–2447, 2004.

[79] V. Wallace, A. Fitzgerald, and E. Pickwell, "Terahertz pulsed spectroscopy of human basal cell carcinoma," *Applied spectroscopy*, Jan. 2006.

[80] Z. Taylor, R. Singh, M. Culjat, J. Suen, W. Grundfest, H. Lee, and E. Brown, "Reflective terahertz imaging of porcine skin burns," *Optics Letters*, vol. 33, no. 11, pp. 1258–1260, 2008.

[81] J.-H. Son, "Terahertz electromagnetic interactions with biological matter and their applications," *Journal of Applied Physics*, vol. 105, no. 10, p. 102033, 2009.

[82] V. P. Wallace and A. J. Fitzgerald, "Terahertz pulsed imaging o of human breast tumors," *Radiology*, vol. 239, pp. 533–540, Apr. 2006.

[83] E. Pickwell, B. E. Cole, A. J. Fitzgerald, M. Pepper, and V. P. Wallace, "In vivostudy of human skin using pulsed terahertz radiation," *Physics in Medicine and Biology*, vol. 49, pp. 1595–1607, Apr. 2004.

[84] H. Hoshina, A. Hayashi, N. Miyoshi, F. Miyamaru, and C. Otani, "Terahertz pulsed imaging of frozen biological tissues," *Applied Physics Letters*, vol. 94, p. 123901, Jan. 2009.

[85] A. Fitzgerald, E. Berry, N. Zinov'ev, S. Homer-Vanniasinkam, R. Miles, J. Chamberlain, and M. Smith, "Catalogue of human tissue optical properties at terahertz frequencies," *Journal of Biological Physics*, vol. 29, no. 2, pp. 123–128, 2003.

[86] K. Cooper, R. Dengler, G. Chattopadhyay, E. Schlecht, J. Gill, A. Skalare, I. Mehdi, and P. Siegel, "A high-resolution imaging radar at 580 GHz," *IEEE Microw. Wireless Compon. Lett.*, vol. 18, no. 1, pp. 64–66, 2008.

[87] K. B. Cooper and G. Chattopadhyay, "Submillimeter-Wave Radar: Solid-State System Design and Applications," *IEEE microwave magazine*, vol. 15, no. 7, pp. 51–67, 2014.

[88] Z. B. Popovic, R. M. Weikle II, M. Kim, and D. B. Rutledge, "A 100-MESFET planar grid oscillator," *Microwave Theory and Techniques, IEEE Transactions on*, vol. 39, no. 2, pp. 193–200, 1991.

[89] R. M. Weikle II, *Quasi-optical planar grids for microwave and millimeter-wave power combining*. PhD thesis, California Institute of Technology, 1992.

[90] R. Eisenhart and P. Khan, "Theoretical and Experimental Analysis of a Waveguide Mounting Structure," *Microwave Theory and Techniques, IEEE Transactions on*, vol. 19, no. 8, pp. 706–719, 1971.

[91] W. A. Shiroma, S. C. Bundy, S. Hollung, B. D. Bauernfeind, and Z. B. Popovic, "Cascaded active and passive quasi-optical grids," *IEEE Trans. Microw. Theory Techn.*, vol. 43, pp. 2904–2909, Dec. 1995.

[92] K. Kurokawa, "Power Waves and the Scattering Matrix," *IEEE Trans. Microw. Theory Techn.*, vol. 13, no. 2, pp. 194–202, 1965.

[93] S. A. Schelkunoff, "Impedance concept in wave guides," *Quarterly of applied mathematics*, 1944.

[94] R. B. Marks and D. F. Williams, "A general waveguide circuit theory," *Journal of Research of the National Institute of Standards and Technology*, vol. 97, no. 5, p. 533, 1992.

[95] J. Stake, L. Dillner, and E. L. Kollberg, "Heterostructure barrier varactors on copper substrate," *Electronics Letters*, vol. 35, no. 4, pp. 339–341, 1999.

[96] P. Goldsmith, *Quasioptical Systems: Gaussian Beam Quasioptical Propogation and Applications*. Wiley-IEEE Press, 1997.

[97] M. A. Morgan and S. Pan, "Graphical Prediction of Trapped Mode Resonances in Sub-mm and THz Waveguide Networks," *IEEE Trans. THz Sci. Technol.*, vol. 3, no. 1, pp. 72–80, 2013.

[98] C.-T. Cheung, J. Hacker, G. Nagy, and D. Rutledge, "A waveguide mode-converter feed for a 5-W, 34-GHz grid amplifier," *Microwave Symposium Digest, 2002 IEEE MTT-S International*, vol. 3, pp. 1523–1526, 2002.

[99] J. B. Hacker, R. M. Weikle II, M. Kim, M. P. DeLisio, and D. B. Rutledge, "A 100-Element Planar Schottky Diode Grid Mixer," *Microwave Theory and Techniques, IEEE Transactions on*, vol. 40, pp. 557–562, Mar. 1992.

[100] T. Bryllert, V. Drakinskiy, K. B. Cooper, and J. Stake, "Integrated 200—240-GHz FMCW Radar Transceiver Module," *IEEE Trans. Microw. Theory Techn.*, vol. 61, no. 10, pp. 3808–3815, 2013.

HBV grid process plan

This document outlines the steps used in the processing of HBV grids.

Process control steps

A	microscope
B	in situ deposition monitoring
C	alfa stepper profile meter, height measurements
D	scanning electron microscopy
E	parameter analyzer
F	coplanar probe measurements with parameter analyser I/V, C/V
G	manual thickness monitor

1. Cleave chips

Use scriber to cleave 19 mm by 19 mm chips from the 3" wafer.

2. Clean chips

Acetone, Methanol, Isopropanol	60°C for 20 min
O_2 plasma strip	100 W for 2 min
Blow dry with N_2^A	

3. Mesa photolithography patterning

Spin resist AZ5214	4000 rpm for 30 s
Soft bake	110°C for 60 s on hot plate
Edge bead exposure	6 mW/cm2 for 60 s
Develop	AZ351B:DI (1:5) for 60 s
Rinse chip in DI and blow dry with N_2	
Pattern exposure	6 mW/cm2 for 6 s
Reversal bake	125°C for 60 s on hot plate
Flood exposure	6 mW/cm2 for 60 s
Develop	AZ351B:DI (1:5) for 25 s
Rinse chip in DI and blow dry with N_2^A	
Ash	90 W O_2 plasma for 20 s

4. Evaporate ohmic contacts

Removal of native oxide	HCl:DI (1:100) for 30 s
Blow dry with N_2	
E-beam evaporating contact metals	10/50/150/200 nm Ni/Ge/Au/Ti evaporation^{B,A}

5. Lift-off

Acetone, Methanol, Isopropanol	60°C for 20 min
Ultrasound acetone bath	60°C
Blow dry with N_2^A	
Height^C	approx. 400 nm
Clean chip from resist remnants	Remover 1165 40 % US @ 60°C for 20 min
Acetone	60°C
Isopropanol	recirculating
DI	autodusch
Blow dry with $N_2^{A,C}$	

6. Rapid thermal anneal

320°C heat cycle for 2 min^{A,C}

7. Dry etch mesas

Methane ICP etching^{A,C,G}	
In-situ monitoring	endpoint detection with laser interferometer
	$Ar_2/H_2/CH_4$ 5/10/5 sccm
	RF:150 W, ICP:500 W
	process pressure 5 mTorr
measure final step height	
Acetone, Methanol, Isopropanol^A	60°C for 10 min
Clean with resist stripper^A	Remover 1165 40 % US @ 60°C for 10 min
Isopropanol, DI^A	
Polymer removal^A	NF_3 RF: 30 W, ICP: 300 W, 80 mTorr for 15 min

8. Post - wet etch

Measure step height before	
Wet etch	H_2SO_4:H_2O_2:DI (1:4:200) for 1 min 30 sec
Measure step height after	
Rinse in DI, blow dry with $N_2{}^{A,C,D}$	

9. Metrology

I/V probe test diodes
SEM verification of etch depth

10. Isolation patterning

Spin resist AZ1512	4000 rpm for 30 s
Soft bake	100°C for 60 s on hot plate
Edge bead exposure	6 mW/cm2 for 60 s
Develop	30 s
Rinse in DI, blow dry with N_2	
Pattern exposure	6 mW/cm2 for 9 s
Develop	20 s
Rinse in DI, blow dry with N_2	
Ash	90 W O_2 plasma for 20 s
Hard bake photoresist	120°C for 30 min in oven
Measure resist step height	

11. Isolation etching

Wet etch	H_3PO_4:H_2O_2:DI (1:1:25) for 10 min
Rinse in DI, blow dry with N_2 [A,C]	
Measure step height of etched + resist	
Remove photoresist	Remover 1165 40 % US @ 60°C for 20 min
Acetone, Methanol, Isopropanol	60°C for 10 min
Blow dry with N_2	
Measure step height of etch	

12. Air bridge support patterning

Put on green tape and spin resist PMGI SF15	30 sec @ 4000 rpm (30 sec 500 rpm ramp)
Soft bake	160°C for 13 min on hot plate
Remove edges with scalpel	
Expose pattern	DUV for 7 min
Develop	PMGI101 for 90 sec
Rinse in DI, blow dry with N_2	
Measure step height of resist	
Ash[A]	50 W O_2 plasma for 1 min

13. Sputter Au seed layer for electroplating

High power sputtering to remove TiOx	RF: 250 W, Ar for 1 min
Sputter seed layer[A]	Ti/Au 10/100 nm

14. Patterning for electroplating with positive thick photoresist

Spin adhesion promotor HDMS	
Spin resist AZ4533	3000 rpm for 30 s
Soft bake	90°C for 115 s on hot plate
Edge bead exposure	6 mW/cm2 for 3 min
Develop	1 min
Rinse in DI, blow dry with N_2	
Pattern exposure	6 mW/cm2 for 15 s
Develop	1 min
Rinse in DI, blow dry with N_2 [A]	
Ash[A]	90 W O_2 plasma for 20 s
Measure step height of resist	

15. Electroplating of airbridges and circuit pattern

Electroplating with 0.5 A/dm^2 with chip on green tape^{A,C,G}	approx. 10 min
Measure thickness several times during plating	
Remove photoresist	cold Acetone for 10 s
Blow dry with N_2	
Ash^A	100 W O_2 plasma for 2 min

16. Remove Au seed layer and photoresist residues

Ion beam milling (IBM)	Ar at 110°, 20 mA, 500 V, for 25 min total
Ash^A	100 W O_2 plasma for 2 min
Remove photoresist	Remover 1165 40 % US @ 60°C for 45 min
Isopropanol	recirculating
DI	automatic rinse with quick drain
Blow dry with N_2^{A,D,E,G}	

17. Patterning with positive thick photoresist for post-etching

Spin adhesion promotor HDMS	
Spin resist AZ4533	3000 rpm for 30 s
Soft bake	190°C for 115 s on hot plate
Edge bead exposure	6 mW/cm2 for 3 min
Develop	1 min
Rinse in DI, blow dry with N_2	
Pattern exposure	6 mW/cm2 for 15 s
Develop	1 min
Rinse in DI, blow dry with N_2	

18. Post-etching of InP for high isolation

Wet etch	HCl:DI (1:1) for 2 min
Rinse in DI, blow dry with N_2^{A,C}	